The Astrophysical Journal Supplement Series, 251:2 (26pp), 2020 November https://doi.org/10.3847/1538-4365/abb607

The Chandra Deep Wide-field Survey: A New Chandra Legacy Survey in the Boötes Field. I. X-Ray Point Source Catalog, Number Counts, and Multiwavelength Counterparts

Alberto Masini[1,2], Ryan C. Hickox[2], Christopher M. Carroll[2], James Aird[3], David M. Alexander[4], Roberto J. Assef[5], Richard Bower[6], Mark Brodwin[7], Michael J. I. Brown[8], Suchetana Chatterjee[9], Chien-Ting J. Chen[10], Arjun Dey[11], Michael A. DiPompeo[2], Kenneth J. Duncan[12,13], Peter R. M. Eisenhardt[14], William R. Forman[15], Anthony H. Gonzalez[16], Andrew D. Goulding[17], Kevin N. Hainline[18], Buell T. Jannuzi[18], Christine Jones[15], Christopher S. Kochanek[19], Ralph Kraft[15], Kyoung-Soo Lee[20], Eric D. Miller[21], James Mullaney[22], Adam D. Myers[23], Andrew Ptak[24], Adam Stanford[25], Daniel Stern[14], Alexey Vikhlinin[15], David A. Wake[26,27], and Stephen S. Murray[15,28]

[1] SISSA, Via Bonomea 265, I-34151 Trieste, Italy; amasini@sissa.it
[2] Dartmouth College, 6127 Wilder Laboratory, Hanover, NH 03755, USA
[3] Department of Physics & Astronomy, University of Leicester, University Road, Leicester LE1 7RJ, UK
[4] Centre for Extragalactic Astronomy, Department of Physics, Durham University, South Road, Durham, DH1 3LE, UK
[5] Núcleo de Astronomía de la Facultad de Ingeniería y Ciencias, Universidad Diego Portales, Av. Ejército Libertador 441, Santiago, Chile
[6] Institute for Computational Cosmology, Department of Physics, University of Durham, South Road, Durham DH1 3LE, UK
[7] University of Missouri, 5110 Rockhill Road, Kansas City, MO 64110, USA
[8] School of Physics and Astronomy, Monash University, Clayton 3800, VIC, Australia
[9] Department of Physics, Presidency University, Kolkata, 700073, India
[10] Marshall Space Flight Center, Huntsville, AL 35811, USA
[11] National Optical Astronomy Observatory, 950 North Cherry Avenue, Tucson, AZ 85719, USA
[12] SUPA, Institute for Astronomy, Royal Observatory, Blackford Hill, Edinburgh, EH9 3HJ, UK
[13] Leiden Observatory, Leiden University, P.O. Box 9513, NL-2300 RA Leiden, The Netherlands
[14] Jet Propulsion Laboratory, California Institute of Technology, 4800 Oak Grove Drive, M/S 169-327, Pasadena, CA 91109, USA
[15] Center for Astrophysics | Harvard & Smithsonian, 60 Garden Street, Cambridge, MA 02138, USA
[16] Department of Astronomy, University of Florida, 211 Bryant Space Center, Gainesville, FL 32611, USA
[17] Department of Astrophysical Sciences, Princeton University, Ivy Lane, Princeton, NJ 08544, USA
[18] Steward Observatory, University of Arizona, 933 North Cherry Avenue, Tucson, AZ 85721, USA
[19] Department of Astronomy, Ohio State University, 140 West 18th Avenue, Columbus, OH 43210, USA
[20] Department of Physics, Purdue University, 525 Northwestern Avenue, West Lafayette, IN 47907, USA
[21] Kavli Institute for Astrophysics and Space Research, Massachusetts Institute of Technology, Cambridge, MA 02139, USA
[22] Department of Physics and Astronomy, The University of Sheffield, Hounsfield Road, Sheffield S3 7RH, UK
[23] Department of Physics & Astronomy, University of Wyoming, 1000 University Avenue, Laramie, WY 82071, USA
[24] NASA/Goddard Space Flight Center, Mail Code 662, Greenbelt, MD 20771, USA
[25] Physics Department, University of California, Davis, CA 95616, USA
[26] Department of Physics, University of North Carolina Asheville, One University Heights, Asheville, NC 28804, USA
[27] Department of Physical Sciences, The Open University, Milton Keynes MK7 6AA, UK
Received 2020 June 23; revised 2020 September 4; accepted 2020 September 6; published 2020 October 22

Abstract

We present a new, ambitious survey performed with the Chandra X-ray Observatory of the 9.3 deg^2 Boötes field of the NOAO Deep Wide-Field Survey. The wide field probes a statistically representative volume of the universe at high redshift. The Chandra Deep Wide-field Survey exploits the excellent sensitivity and angular resolution of Chandra over a wide area, combining 281 observations spanning 15 yr, for a total exposure time of 3.4 Ms, and detects 6891 X-ray point sources down to limiting fluxes of 4.7×10^{-16}, 1.5×10^{-16}, and 9×10^{-16} erg cm^{-2} s^{-1} in the 0.5–7, 0.5–2, and 2–7 keV bands, respectively. The robustness and reliability of the detection strategy are validated through extensive, state-of-the-art simulations of the whole field. Accurate number counts, in good agreement with previous X-ray surveys, are derived thanks to the uniquely large number of point sources detected, which resolve 65.0% ± 12.8% of the cosmic X-ray background between 0.5 and 2 keV and 81.0% ± 11.5% between 2 and 7 keV. Exploiting the wealth of multiwavelength data available on the field, we assign redshifts to ∼94% of the X-ray sources, estimate their obscuration, and derive absorption-corrected luminosities. We provide an electronic catalog containing all of the relevant quantities needed for future investigations.

Unified Astronomy Thesaurus concepts: Catalogs (205); X-ray active galactic nuclei (2035); X-ray astronomy (1810); Active galactic nuclei (16); AGN host galaxies (2017)

Supporting material: FITS file

1. Introduction

It is now widely accepted that the large majority of massive galaxies in the observable universe host supermassive black holes (SMBHs) in their nuclei, with masses ranging between

[28] Steve Murray passed away on 2015 August 10. This survey would not have been possible without his invaluable contribution.

10^6 and 10^{10} $M_\odot$ (Kormendy & Ho 2013). The evidence is provided by multiple observations, such as tracing the kinematics and dynamics of stars in the central region of the Milky Way (e.g., Ghez et al. 2008) and the bulges of nearby galaxies (Kormendy & Richstone 1995; Kormendy 2004), water megamasers (Kuo et al. 2011), and the recent direct imaging of the shadow of the SMBH in M87 (Event Horizon Telescope Collaboration et al. 2019).

Studies of SMBHs have gained increasing importance in recent decades, subsequent to the discovery of scaling relations connecting the masses of SMBHs to properties of their host galaxy bulges, such as bulge luminosity (Magorrian et al. 1998), mass (Häring & Rix 2004), and stellar velocity dispersion (Ferrarese & Merritt 2000; Gebhardt et al. 2000), suggesting a coevolution of the two. In particular, there must be some connection between the growth of the SMBH (which happens through direct accretion of matter and presumably through mergers) and the mass growth of the environment in which it resides (i.e., as traced by star formation).

At any given time, the majority of SMBHs lie dormant, but a small fraction are known to emit a significant amount of light and energy, often outshining the whole host galaxy across the electromagnetic spectrum, resulting in an active galactic nucleus (AGN). The AGNs are powered by the release of gravitational energy from matter accreted onto the SMBHs in the nuclei of galaxies. The large energy released by an AGN can effectively influence its surrounding environment, eventually impacting the whole bulge/nuclear region, as well as the star formation and the evolution of the galaxy as a whole (see, e.g., Harrison 2017, for a recent review). Strong observational evidence of AGN feedback (e.g., Fabian 2012) has shown that AGNs are responsible for the observed correlations between the mass of inactive SMBHs and host galaxy properties. The similarity of the cosmic star formation and SMBH accretion rate histories, both peaking in the same redshift range ($z \sim 2$; see Madau & Dickinson 2014, for a review), provides an additional piece of evidence that the two phenomena are linked, although many details are still missing.

Indeed, despite AGNs now being much-studied, many compelling questions remain unanswered, given the difficulty of investigating causal links between phenomena that span a large range of spatial and temporal scales (e.g., accretion happens on microparsec scales, while feedback occurs on kiloparsec scales). Studying and solving these cosmic puzzles is further complicated by differences in the environment, cosmic epoch, luminosity, morphology, color, and mass of the galaxies considered; the obscuration state of the AGN; and so on.

Thus, while a generally accepted picture of AGN–galaxy coevolution has emerged through the years, the exact details of how AGNs impact the overall galaxy population are still elusive. Large, statistically robust samples of AGNs can help address the open questions and potentially lead to new discoveries. However, particular care has to be paid to the different selection methods; it is now well established that AGNs selected with radio, IR, optical, and X-ray observations probe broadly different samples of the underlying parent population of AGNs (Hickox et al. 2009). Moreover, despite their significant luminosity, the effects of obscuration by dust and gas and dilution by the light of the stars of the host galaxy severely hamper any unbiased selection of large statistical samples (Hickox & Alexander 2018). Usually, the X-ray energy band is considered to be the most reliable in detecting accreting SMBHs, due to high contrast with the host galaxy and the high penetrating power of X-ray radiation (Brandt & Alexander 2015). However, even X-ray-selected samples suffer some bias against obscured sources and heavily rely on multiwavelength data to derive redshifts (either spectroscopic or photometric), luminosities, and host galaxy properties, such as the stellar mass and star formation rate.

Over the last few decades, the large majority of X-ray telescopes have undertaken an ever-growing number of X-ray surveys of the sky, covering large portions of the flux-area plane. A given exposure time can be spent staring for a long time at a small area of the sky (e.g., what has been done for the Chandra deep fields; see Xue 2017, for a review) to detect extremely faint X-ray sources or spread over a larger area at the cost of missing the faintest sources to obtain better statistics for bright sources. Ideally, a combination of deep pencil-beam and shallow wide surveys is key to probe the largest portion of the parameter space in terms of AGN luminosity, accretion rate, redshift, and obscuration state.

The majority of the more extensive Chandra surveys have been updated in the last decade, pushing observations to either deeper flux limits (e.g., accumulating up to 7 Ms of time in the Chandra Deep Field South; Luo et al. 2017; Xue 2017) or wider areas (e.g., extending the Chandra coverage in COSMOS, from the C-COSMOS to the Chandra COSMOS Legacy Survey; Elvis et al. 2009; Civano et al. 2016). One such survey, the NOAO Deep Wide-field Survey (NDWFS) Boötes field, has, however, lagged behind in sensitivity.

Subsequent to the first extensive XBoötes survey (Kenter et al. 2005; Murray et al. 2005) more than 15 yr ago, the NDWFS Boötes field has been observed multiple times but in a heterogeneous way. So an additional large program was scheduled to cover the central 6 $\deg^2$ of the field with more than 1 Ms of Chandra time. These observations were designed to push the detection limit to significantly fainter sources and upgrade the Boötes field to better match other state-of-the-art surveys. In this paper, we present the Chandra Deep Wide-Field Survey (CDWFS), which, given its optimal combination of sensitivity and survey area, significantly improves the discovery space in the flux limit–survey area plane (see, e.g., Figure 1 of Xue 2017 and Figure 3 of Brandt & Alexander 2015). We exploit the full extent of the Chandra data in the NDWFS Boötes field, homogeneously analyzing the plethora of available observations, to produce a new, high-quality data set that will serve as a base for future scientific discoveries.

The paper is structured as follows. We present in detail the data reduction and preparation in Section 2. In Section 3, we describe the methodology adopted to build and exploit simulations of the whole CDWFS data set. Once the probability thresholds are calibrated, the production of the X-ray catalog is presented in Section 4. The large number of X-ray point sources is used to derive accurate number counts in Section 5, while Section 6 describes the procedure used to assign multiwavelength counterparts and redshifts to our X-ray sources. In the same section, we also derive hardness ratios (HRs), column densities, and deabsorbed rest-frame luminosities. A brief description of each column in the catalog is given in Section 7. The future potential of CDWFS is summarized in Section 8.

Table 1
Description of the First 10 Chandra Observations Considered in This Work

ObsID	R.A. (deg)	Decl. (deg)	Roll (deg)	Exposure (ks)	MJD	Cycle
3130	216.408	35.600	163.4	119.9	52,380.1	3
3482	216.407	35.596	219.9	58.5	52,434.2	3
3596	219.751	35.702	141.0	4.6	52,735.0	4
3597	219.321	35.702	141.0	4.6	52,734.5	4
3598	218.891	35.702	141.0	4.7	52,733.1	4
3599	218.461	35.702	141.0	4.6	52,732.2	4
3600	218.031	35.702	141.0	4.7	52,730.5	4
3601	217.601	35.702	141.0	4.5	52,736.1	4
3602	217.171	35.702	141.0	4.5	52,735.0	4
3603	216.742	35.702	141.0	4.7	52,725.4	4

Note. The full version can be found in the electronic version of the journal. (This table is available in its entirety in FITS format.)

To derive luminosities, we assume a flat ΛCDM cosmology with $H_0 = 70\,\mathrm{km\,s^{-1}\,Mpc^{-1}}$ and $\Omega_M = 0.3$.

2. Data Reduction

The NDWFS Boötes field (Jannuzi & Dey 1999), centered on coordinates (J2000) of R.A. = 14:32:05.712, decl. = +34:16:47.496, has been extensively observed by Chandra over more than 15 yr of operations. Many additional pointings complemented the two most intensive runs of observations, the XBoötes survey performed during Chandra's Cycle 3 (Kenter et al. 2005; Murray et al. 2005) and the recent large program in Cycle 18 (PI: R. Hickox).

To fully exploit the huge amount of information on the same area of the sky, we collected all 281 Chandra pointings in the Boötes field conducted between 2003 and 2018, all in VFAINT mode. A log showing the first 10 observations included in this work can be found in Table 1 (the complete list of observations is available in electronic format).

2.1. Astrometric Correction

The 281 Chandra observations were downloaded from the Chandra Data Archive[29] and reduced with CIAO 4.11 (Fruscione et al. 2006) and CALDB version 4.8.2.

After reprocessing the data with the task `chandra_repro` with the flag `check_vf_pha=yes`, the observations were aligned. First, we ran the source detection tool `wavdetect` on each observation, adopting a permissive threshold (using three scales of ($\sqrt{2}$, 2, 4) pixels and setting the number of allowed spurious sources per scale to be `falsesrc` = 3, i.e., allowing for ∼10 spurious sources per field). Then, we matched sources within 6′ of the aimpoint (where the Chandra point-spread function (PSF) is approximately circular) to the catalog of optical counterparts to the XBoötes sources of Brand et al. (2006)[30] using the task `reproject_aspect`. This task rotates and translates an observation to minimize the difference between the positions of the X-ray sources and the reference list of optical counterparts. The `reproject_aspect` task requires at least three sources in common between the X-ray and optical catalogs to solve for both a rotation and a translation. Six of our observations had fewer than three X-ray/optical sources in common. For these, we used `method=trans` instead of the default method. This flag forces `reproject_aspect` to use only translation transformations and requires a minimum of one common source. The data were then reprocessed using the new aspect solution files. The results of this calibration step are shown in Figure 1, which demonstrates how the calibration adjusts and narrows the source distribution: 68% of the data are matched within 0.″7, 90% within 1.″2, and 95% within 1.″5. Of course, this approach relies upon the correct identification of optical counterparts to XBoötes sources; however, the width of the histograms in Figure 1 is consistent with being largely dominated by X-ray positional uncertainties. We tested that a pure X-ray alignment of the observations (i.e., not relying on optical counterparts but employing common X-ray sources detected in partially overlapping observations) requires the use of very off-axis sources due to the scarcity of overlap for many observations, hampering the accuracy of the astrometric correction. The large exposure time range for partially overlapping observations further complicates the feasibility of such an alignment on the whole 9.3 deg^2 area.

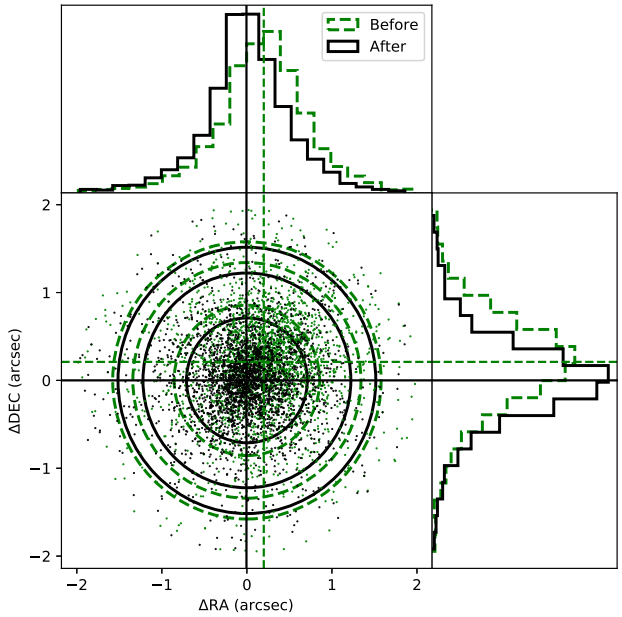

Figure 1. Distribution of the difference in R.A. and decl. between X-ray and optical sources before (green points and dashed lines) and after (black points and solid lines) the astrometric correction. The three circles represent the radii at which 68%, 90%, and 95% of the sources are enclosed, respectively. The alignment centers the distributions on zero and makes them narrower. As a result, the CDWFS observations are aligned with the NDWFS astrometry.

The described procedure aligned the X-ray observations to the world coordinate system (WCS) of the NDWFS Boötes field, which is the USNO-A2 one. As noted by Cool (2007), the USNO-A2 WCS could have a systematic shift with respect to more recent ones. Thus, we decided to register all of the data and catalogs that we are going to use throughout this paper to the same astrometric reference, the most recent being the one provided by the Gaia mission (Gaia Collaboration et al. 2016). Cross-matching USNO-A2 with Gaia DR2 (Gaia Collaboration et al. 2018) in the same region of the sky, encompassing the whole Boötes field, we found a systematic shift of $\mathrm{R.A._{NDWFS}} - \mathrm{R.A._{Gaia}} = 0.''32$ and $\mathrm{decl._{NDWFS}} - \mathrm{decl._{Gaia}} = 0.''20$. After checking that the shift is consistent throughout the field, we applied the appropriate astrometric correction to all of our mosaics. On the other hand,

[29] https://cda.harvard.edu/chaser/
[30] This implies that the optical sources are counterparts to previously detected XBoötes sources with at least four counts.

the Spitzer data of the Boötes field that we are going to use in this paper did not show any coordinate shift with respect to Gaia's astrometry. We refer the interested reader to Appendix A for a detailed discussion of the astrometry and coordinate registration.

2.2. Flare Filtering

We cleaned our observations of time intervals with high background using the tool `dmextract` to create 0.5–7 keV band light curves and `lc_sigma_clip` to create a good time interval (GTI) file after applying 3σ clipping to the light curve. We then used `dmcopy` to filter our event files using the GTI files.

This procedure resulted in a minimal time loss of 31 ks over 3.4 Ms of data (less than 1%). We also note that, as reported by Murray et al. (2005), six XBoötes observations (i.e., ObsIDs 3601, 3607, 3617, 3625, 3641, and 3657) had a higher background compared to the others. These observations were not discarded, consistent with the procedure of Murray et al. (2005). In addition to these observations, the short (6.1 ks) ObsID 17423 suffered from flaring but was not discarded. The inclusion of these seven observations is expected to have a negligible impact on the detection of sources given their relatively short exposure.

2.3. Exposure Map Creation

Exposure maps were created with the `fluximage` task. In this work, we adopt the following Chandra bands: full or broad (*F*; 0.5–7.0 keV), soft (*S*; 0.5–2.0 keV), and hard (*H*; 2.0–7.0 keV). When run in its default mode, `fluximage` produces vignetting-corrected exposure maps in units of cm^2 s counts photon^{-1}, while if the tool is run with the parameter `units = time`, the effective area of the Chandra mirrors is ignored. To obtain vignetting-corrected exposure maps with units of seconds, we produced effective area maps running `fluximage` with `units = area` (i.e., units of cm^2 counts photon^{-1}) and then divided each default exposure map by the maximum value of its corresponding effective area map.

Since the exposure map is theoretically monochromatic, it is computed at a given effective energy. The effective energies adopted in this work are 2.3, 1.5, and 3.8 keV for the *F*, *S*, and *H* bands, respectively. The *F*-band exposure map of the whole field is shown in Figure 2. All of the mosaics used in this work were created with the CIAO task `reproject_image` and spatially rebinned by a factor of 4 to speed up the computation time. This means that each pixel of the 4×4 rebinned mosaics has a scale of $1\farcs968$. A false-color image of the whole field is shown in Figure 3.

2.4. Background Map Creation

Precise background maps are crucial to having a reliable detection strategy and building accurate simulations. The quiescent (i.e., nonflaring) Chandra background can be explained, to first order, by the sum of an instrumental and an astrophysical component. The instrumental background is due to particles mimicking the signal of X-ray photons and to nonastrophysical X-ray photons, such as the ones produced by the interactions of particles with the spacecraft structure. The astrophysical background is the contribution from unresolved X-ray sources, mostly AGNs, that are fainter than the flux limit of each observation (i.e., the so-called cosmic X-ray

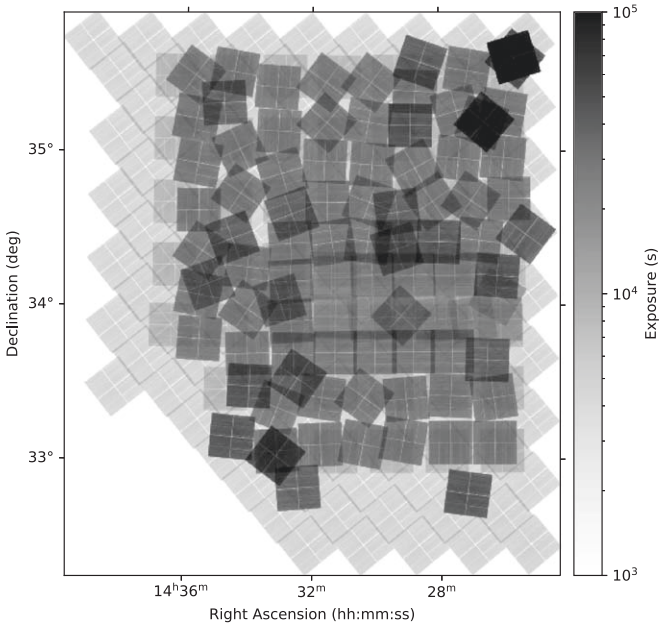

Figure 2. The exposure map of the whole Boötes field shows the 281 overlapping observations considered in this work, as well as the large dynamic range in exposure involved. The external part of the field shows the observations of the XBoötes survey at broadly ∼5 ks of exposure (light gray), while the Chandra Cycle 18 large program (darker gray) pushes the central 6 deg^2 of the field to ∼30 ks of depth. Other deep pointed observations (black) are also included.

background (CXB)). In addition, there is also diffuse emission of mainly soft X-rays from various local components, such as the Local Bubble and solar wind charge exchange mechanism (Markevitch et al. 2003; Slavin et al. 2013). Although the Chandra background is generally very low, the large dynamic range in exposure times over our field requires a careful disentangling of the two components for each observation; indeed, while the instrumental background is unvignetted, the astrophysical component is vignetted, band-dependent (the diffuse soft emission has a minor contribution in the hard band), and exposure-dependent (i.e., the fraction of unresolved sources, hence the CXB contribution, becomes smaller in deeper exposures).

We started by creating instrumental background maps following the procedure of Hickox & Markevitch (2006). Briefly, since the Chandra effective area rapidly decreases at $E > 9$ keV, the 9–12 keV band is vastly dominated by instrumental background. We then extracted the number of counts per pixel and per second in the 9–12 keV band with `dmextract`. The Chandra instrumental background is well known to be anticorrelated with the solar cycle (e.g., Markevitch et al. 2003)[31]; thanks to the large time span of our observations (∼15 yr), we were able to see this trend on more than one full solar cycle, as shown in Figure 4. This also confirmed the vastly nonastrophysical nature of the events in the 9–12 keV band; their number could thus be converted to

[31] The actual causes of the anticorrelation are complicated and still debated. The flux of the particle background is likely modulated by both the solar wind speed and the solar magnetic field (Ross & Chaplin 2019, and references therein); when the solar activity is higher, the cosmic-ray modulation is driven by disturbances in the solar wind (and hence in the heliospheric current sheet). It is likely that these disturbances result in a lower incidence of particle background on Chandra's FOV as well during solar maxima.

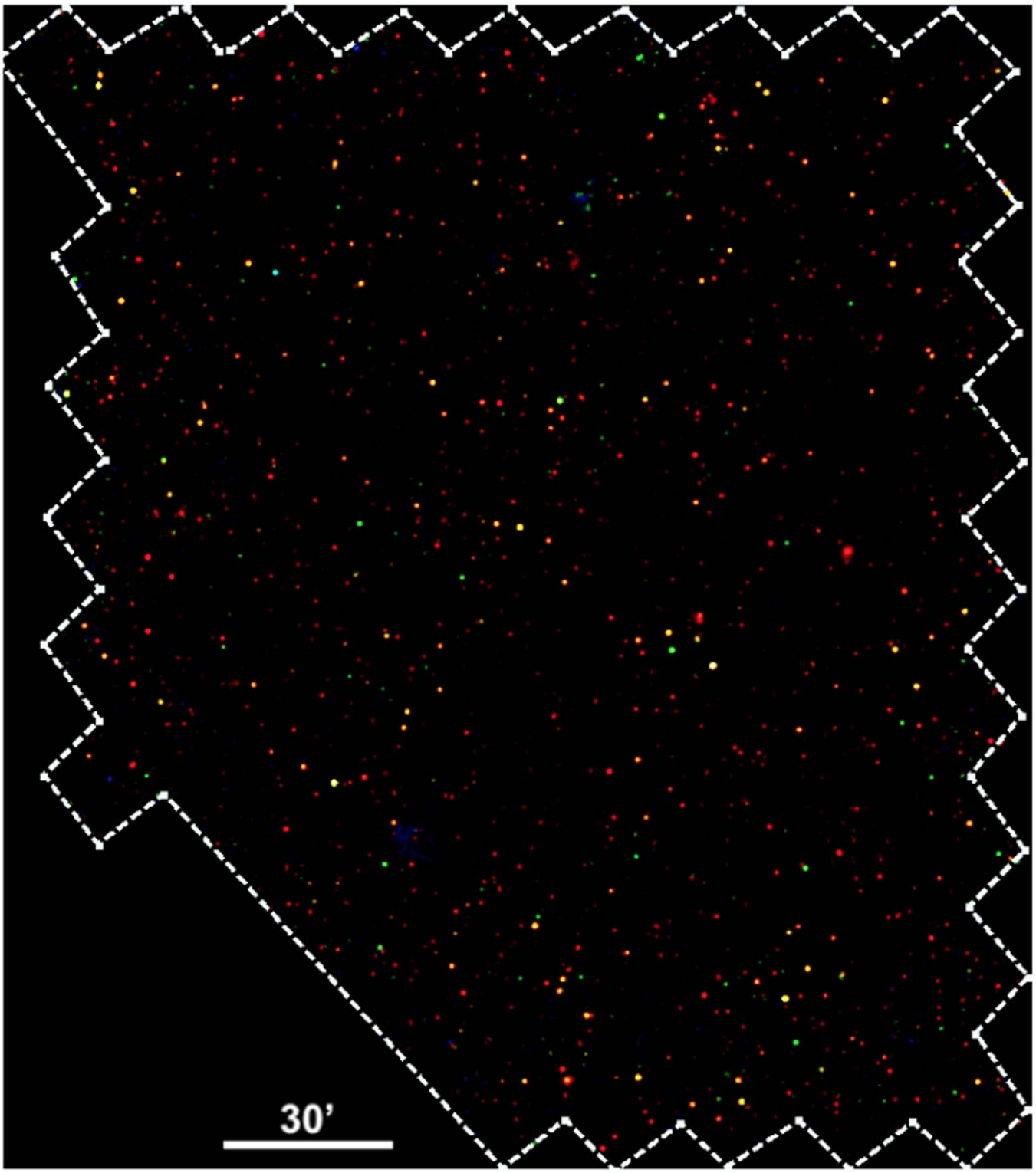

Figure 3. False-color image of the whole Boötes field as observed by Chandra, for illustration purposes only. We mapped the 0.5–2 keV band as red, 2–4.5 keV as green, and 4.5–7 keV as blue. Due to the large size of the field, we smoothed the whole image with a Gaussian filter of 20 pixels (i.e., $39\farcs36$) in radius, and both the scale and color bar were adjusted to enhance the contrast and color of the sources. Due to the large dynamic range in exposure and heavy smoothing, many sources in the deeper part of the field and with a smaller PSF are not clearly visible. The dashed white line delimits the field, while the solid white segment labels $30'$. North is up and east on the left.

instrumental background counts in other bands. Hickox & Markevitch (2006) estimated that the ratios between instrumental background in the *F*, *S*, and *H* bands and the one in 9–12 keV are 1.52, 0.4, and 1.12, respectively. Using these ratios, the total number of counts in the *F*, *S*, and *H* bands attributed to instrumental background could be obtained ($B_{\rm Instr}$)

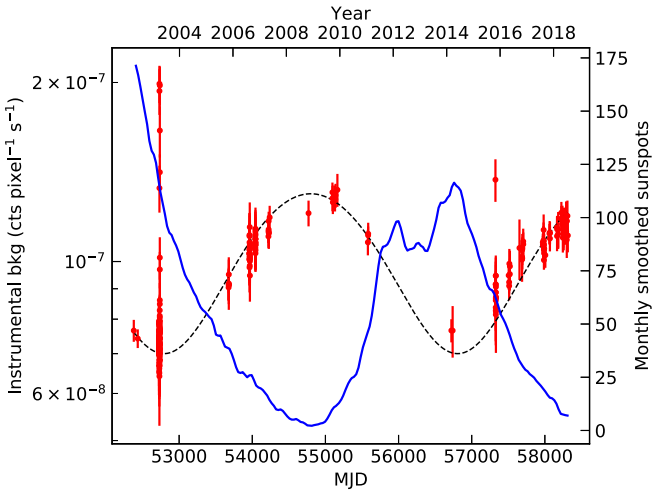

Figure 4. Chandra instrumental background surface brightness (in counts per pixel per second) as a function of modified Julian date (MJD; bottom axis) and, as a reference, year (top axis). The XBoötes observations during 2003 are seen on the left, where the small number of flared exposures as reported in the text and by Kenter et al. (2005) are visible as outliers. The outlier on the right is another flared short exposure (∼6 ks; ObsID 17423), which also was not discarded. The dashed black line marks a sinusoid with a period of 11 yr, and it is not a fit to the data. It has been tuned to have a peak and minimum at the approximate start and maximum of solar cycle 24, respectively. The solar activity is represented by the monthly smoothed sunspot number (blue line; SILSO World Data Center 2002–2018), whose trend clearly shows an anticorrelation with the instrumental background surface brightness.

and compared to the total number of counts extracted from the data ($B_{\rm Data}$). To estimate the background directly from the data, for each observation, we extracted photons from a 6′ radius circular area centered on the aimpoint, appropriately masking out point sources detected in a given band with significance $>3.5\sigma$ and clusters from the catalog of Kenter et al. (2005). The counts extracted from the central 6′ were then redistributed homogeneously over the whole field of view (FOV), rescaling by the ratio between the number of pixels of the ACIS-I FOV and those of the extraction area. Then, for each observation, we compared the number of background counts extracted from the data with the counts estimated from the instrumental background alone: if the difference $B_{\rm Data}$–$B_{\rm Instr}$ was positively above 3σ (meaning that the data contained a significant number of excess counts of astrophysical nature), we subtracted the instrumental background from the total one, vignetted the resulting difference, and summed this component to the instrumental map to obtain the total background map ($B_{\rm Tot}$). Otherwise, the background from the data was considered consistent within 3σ with the instrumental background map previously created.

In Figure 5, we show the distribution of the differences (in σ) $B_{\rm Data}$–$B_{\rm Instr}$ before applying any correction (orange dashed histogram) and $B_{\rm Data}$–$B_{\rm Tot}$ after taking into account the CXB and soft diffuse emission (blue solid histogram), as well as their Gaussian fits (orange and blue dashed lines, respectively). As can be seen from Figure 5, the blue histograms are centered on zero and narrower than the orange ones. In the hard band, the distributions are very similar, implying that the background is mostly instrumental, and our extrapolation of the instrumental background from the 9–12 keV band was able to explain the background in our data in the majority of the observations.

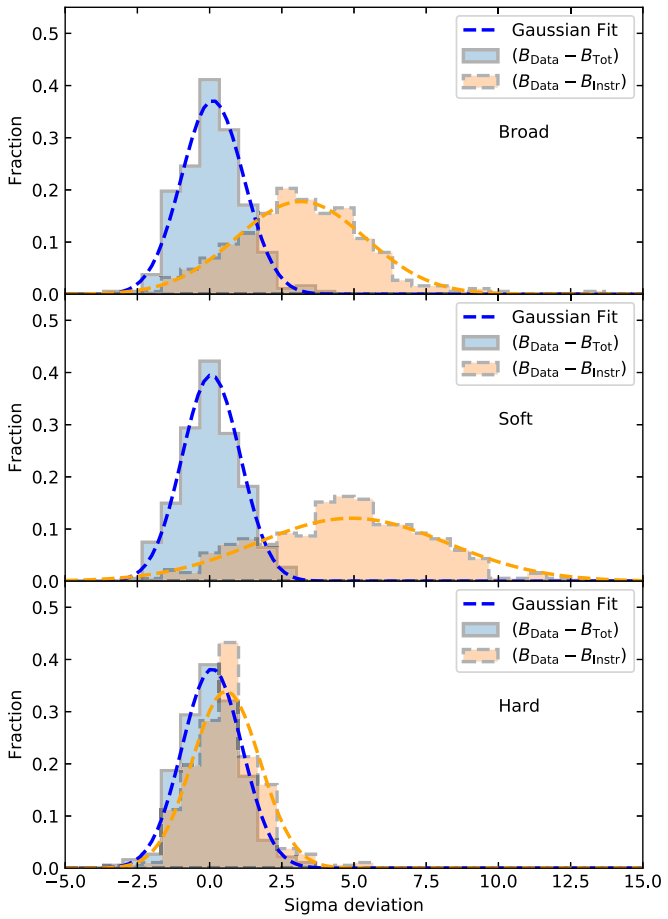

Figure 5. Distributions of the counts difference between $B_{\rm Data}$ and $B_{\rm Instr}$ (before applying any correction to our background maps; orange dashed histogram) and between $B_{\rm Data}$ and $B_{\rm Tot}$ (after adding the CXB and soft diffuse emission; blue solid histogram). The dashed orange and blue lines are Gaussian fits to the two distributions. This figure shows that the final background maps we used in this work are consistent with the background extracted from the data.

2.5. PSF Map Creation

Chandra's PSF is known to be spatially and energy dependent. In particular, the farther away from the aimpoint and the higher the energy, the larger the size. The shape of the PSF also varies across the FOV with the azimuthal angle, significantly deviating from a circular shape and becoming more and more elliptical. However, the usual way to approximate this behavior is by defining the radius that encircles 90% of the energy, r_{90}. An approximate formula widely used in the literature (e.g., Hickox & Markevitch 2006) based on the trend of the PSF size with the off-axis angle θ shown in the Chandra Proposers' Observatory Guide[32] is

$$r_{90} \approx \begin{cases} 1'' + 10''(\theta/10')^2, & E = 1.5\ \text{keV} \\ 1\farcs8 + 10''(\theta/10')^2, & E = 6.4\ \text{keV}. \end{cases} \quad (1)$$

Using this approximate formula for r_{90}, we multiplied the computed value of r_{90} in each pixel with the vignetting-corrected exposure map at the same pixel. We created maps of $r_{90} \times t_{\rm Exp}$ and $r_{90}^2 \times t_{\rm Exp}$, then merged all of the observations together and divided the resulting mosaics for the total exposure map mosaic. This can be mathematically expressed

[32] http://cxc.harvard.edu/proposer/POG/pdf/MPOG.pdf

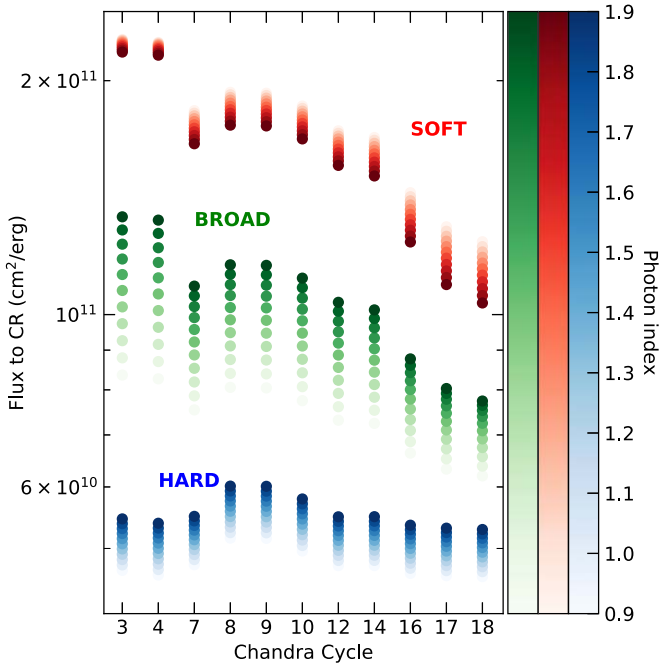

Figure 6. The ECFs, from flux to count rate, as a function of Chandra cycle and color-coded by photon index. The green, red, and blue color maps refer to the *F*, *S*, and *H* bands, respectively. Taking into account the temporal variation of the instrument is crucial for building accurate simulations.

(for r_{90}) as $\sum_{i=1}^{N} r_{90,i} t_{\mathrm{Exp,i}} \Big/ \sum_{i=1}^{N} t_{\mathrm{Exp,i}}$, where the sum is over the overlapping observations contributing to each pixel. This procedure effectively returned two mosaics of an exposure-weighted average of r_{90} and r_{90}^2. While the former mosaic was used extensively in the following analysis to extract aperture photometry, the latter one was used to derive the sensitivity of the survey (Section 3.2).

2.6. Energy Conversion Factor Map Creation

The large time span of our observations across 15 yr of Chandra operation (between Chandra's Cycles 3 and 18), during which the spacecraft's effective area significantly changed, implies that the same intrinsic flux, spectral shape, and exposure time will result in a different number of counts detected in different positions on the field.

We used PIMMS as part of the Chandra Proposal Planning Toolkit[33] to obtain the energy conversion factors (ECFs) in the three energy bands adopted and for all of the Chandra cycles considered in this work (3, 4, 7, 8, 9, 10, 12, 14, 16, 17, and 18) and a range of photon indexes centered on $\Gamma = 1.4$, which is the average photon index of the populations of AGNs mostly making up the unresolved CXB spectrum (De Luca & Molendi 2004; Hickox & Markevitch 2006). Figure 6 graphically shows the significant evolution of the ECFs across the years, mainly in the soft band and seen regardless of the adopted spectral shape.

To create an ECF mosaic of the field, we first created the single maps. For each observation, we considered the ECF given by its Chandra cycle, assuming a power law with photon index $\Gamma = 1.4$ and Galactic absorption $N_{\mathrm{H,\,Gal}} = 1.04 \times 10^{20}$ cm^{-2} (Kalberla et al. 2005), and convolved the appropriate ECF with the vignetting-corrected exposure map. Then, analogous to what was done for the PSF maps, we merged the observations to create a mosaic and divided the latter by the total exposure map mosaic.

3. Simulations

In the original XBoötes survey, thanks to a remarkably uniform and low background, a simple cut in total counts could efficiently limit the number of spurious sources. When combining observations from different cycles and with vastly different exposures, however, such a cut is not optimal, and the probability of being a spurious background fluctuation has to be carefully evaluated for each source.

An effective strategy to approach this problem is to perform simulations of the observed data. To have full control of the numerous variables playing a role in a robust source detection, we decided to perform a full simulation of the entire Boötes field.

The starting point is to assume a reasonable distribution for the number of sources per flux bin and unit area (i.e., a differential number counts distribution, dN/dS). We assumed the Lehmer et al. (2012) dN/dS in the *F*, *S*, and *H* bands separately, defined a range of fluxes (extending down to $\sim 5 \times 10^{-17}$ erg cm^{-2} s^{-1}, a factor of 20 lower than the expected flux limit), and made a Poissonian realization of the dN/dS at each flux, creating the input list of sources. Each source was then assigned a random set of coordinates (R.A. and decl.) accounting for the curvature of the sky.[34] Each source was also assigned a photon index Γ between 0.9 and 1.9 drawn from a Gaussian probability distribution with $\mu = 1.4$ and $\sigma = 0.2$. When producing simulated sources, we did not account for the fact that the real sources might be clustered.[35]

For each observation, we considered only those input sources falling on its FOV. Then, the coordinates of each source (R.A. and decl.) were converted with the tool `dmcoords` into θ and ϕ (the distance in arcminutes of the given position from the aimpoint and its azimuthal angle). These two quantities are crucial to take into proper account the effect of the variation of Chandra's PSF on the FOV. We used these coordinates to access the correct PSF image,[36] renormalize the image to have the expected number of counts given the input flux,[37] and place it on the instrumental background. The significant number of sources below the flux limit ensured that a similar effect for the CXB was naturally produced by undetectable sources. This procedure was performed for all observations (adopting the same observational configuration for each), which were then merged together. The final simulation is then a Poissonian realization, pixel by pixel, of the whole mosaic.

[33] http://cxc.harvard.edu/toolkit/pimms.jsp

[34] While the R.A. was assigned randomly, the randomly chosen decl. was accepted only if $\cos(\mathrm{decl.} \times \pi/180) > P$, where P is a random number uniformly drawn between zero and 1. This (small) effect is introduced to more densely populate the low decl. area of the field.

[35] The choice of the photon index range has a negligible impact on the result of the simulations, as we have tested that injecting sources with a fixed $\Gamma = 1.4$ gives consistent results. This is not completely surprising, since the main goal of the simulations is to study the occurrence of background fluctuations as a function of probability threshold. For the same reason, we do not believe that any missing clustering signal in the simulations significantly impacts our conclusions.

[36] The images of the PSF are stored in a file with a discrete range of elevations and azimuths, where $\mathrm{elev} = \theta \sin\phi$ and $\mathrm{azim} = \theta \cos\phi$.

[37] Each source has its own randomly chosen photon index, which translates to a different ECF. In summary, we have a different ECF for any Chandra cycle, photon index, and energy band employed.

Source detection was performed following a standard approach, extensively applied in the literature for many X-ray surveys (e.g., Nandra et al. 2005, 2015; Laird et al. 2009; Xue et al. 2011; Civano et al. 2016). Sources were detected on the whole simulated mosaic with `wavdetect`, using the exposure map mosaic (with the parameter `expthresh` = 0.01) and the PSF map mosaic (the mosaic of exposure-averaged r_{90}) as additional inputs. We chose a permissive threshold `sigmathresh` $= 5 \times 10^{-5}$, analogous to what was done for XBoötes, and scales of ($\sqrt{2}$, 2, 4) pixels.[38] The source list returned by `wavdetect` was expected to contain many spurious sources due to the permissive threshold adopted, while at the same time being very complete.

We then performed aperture photometry at the position of each source returned by `wavdetect` using the average r_{90} at that position and extracting total and background counts and the average vignetting-corrected exposure. Each source was assigned a probability of being spurious, i.e., the Poissonian probability that the observed total counts are entirely due to the expected background. Net (i.e., background-subtracted) counts (N) were then converted to count rates ($\mathrm{CR} = 1.1N/t_{\mathrm{Exp}}$, where the factor 1.1 corrects for the encircled energy fraction of the PSF) and finally to fluxes through the ECF map mosaic, recalling that the mosaics were created assuming a single photon index $\Gamma = 1.4$. Uncertainties were computed following Gehrels (1986).

As a final step, the list of sources was cleaned for possible multiple detections of single bright sources whose PSF wings can be independently detected. Feeding the PSF map mosaic to `wavdetect` helped to drastically reduce the number of such spurious detections (to less than 0.05%). When two sources were detected within the size of the PSF at that position, we retained the most significant one.

We have tested a wide range of simulations: altering the precise shape of the input dN/dS, assigning the same and different photon indices to all sources, changing the `wavdetect` input parameters, and running a set of 10 realizations for each band and set. The results are consistent among each of the simulations. We also generated three independent lists of input sources, with a corresponding set of 10 different Poissonian realizations. In the rest of this section, we discuss the tests that use this total set of 30 simulations for each energy band.

3.1. Setting a Probability Threshold

As already mentioned, the list of sources returned by `wavdetect` was expected to be highly complete but, at the same time, include a significant number of spurious detections. Using a reasonable and justifiable probability threshold can drastically reduce the spurious fraction.

The total number of spurious sources detected in a simulation depends on Poisson statistics, the magnitude of the background, and the parameters of the detection algorithm (such as the `sigmathresh` and `scales` parameters of `wavdetect`). As long as the background used in the simulations is an accurate representation of the real background, and the detection process is the same as that adopted to detect sources in the real data, we can expect the number of spurious sources to be consistent within different realizations.

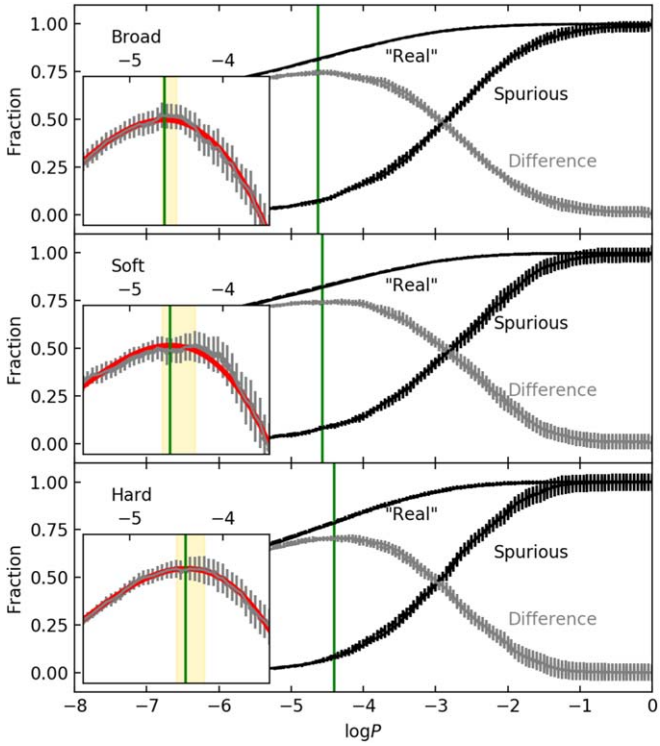

Figure 7. Distributions of the fraction of matched and unmatched sources for the three sets of simulations (black points and error bars) and their difference (gray points and error bars) as a function of logarithmic probability, $\log P$, for the three bands (from top to bottom, F, S, and H). Each point is obtained by cutting the catalogs at the given $\log P$ and counting how many sources are/are not matched to their input counterparts. Cutting the catalog at a higher $\log P$, more and more sources are detected but not matched to any input source. The green line labels the probability threshold that maximizes the difference between matched and unmatched sources, obtained by fitting the peak range with a third-degree polynomial (red line in the insets, which show zoom-ins of the peak regions). The fitted positions of the peaks are consistent with the range defined by the single simulation sets (yellow region in the insets).

Spurious sources are, by definition, sources returned by `wavdetect` that do not correspond to a "real" input source. The fraction of spurious sources increases toward high probability (i.e., toward $\log P \sim 0$), with a tail of fewer spurious sources being assigned a lower probability. We can use our simulated sources to compare the relative fraction of matched (i.e., real) and unmatched (i.e., spurious) sources at each probability. We expect these normalized distributions to have different shapes, so that we can determine a probability threshold that maximizes the difference between the two. This is shown in Figure 7, where it can be seen that around $\log P \sim -4.5$, the difference between the two distributions is maximal. Due to statistical noise, the three sets of simulations (with different input sources) return slightly different peaks, as indicated by the yellow regions in Figure 7. Since setting an accurate probability threshold is crucial for this work, we computed the median of the three "Difference" curves in Figure 7 and fitted it with a third-degree polynomial function over the range $-6 < \log P < -3$. The fits are shown in the insets in Figure 7. The final thresholds we determined to minimize the selection of spurious sources are $\log P = (-4.63, -4.57, -4.40)$ for the F, S, and H bands, respectively.

[38] We tested that adding an additional 8 pixel scale did not significantly change the results in terms of number of detected sources. The reliability thresholds determined through simulations were consistent with the ones we used in the main text, resulting in slightly fewer sources robustly detected.

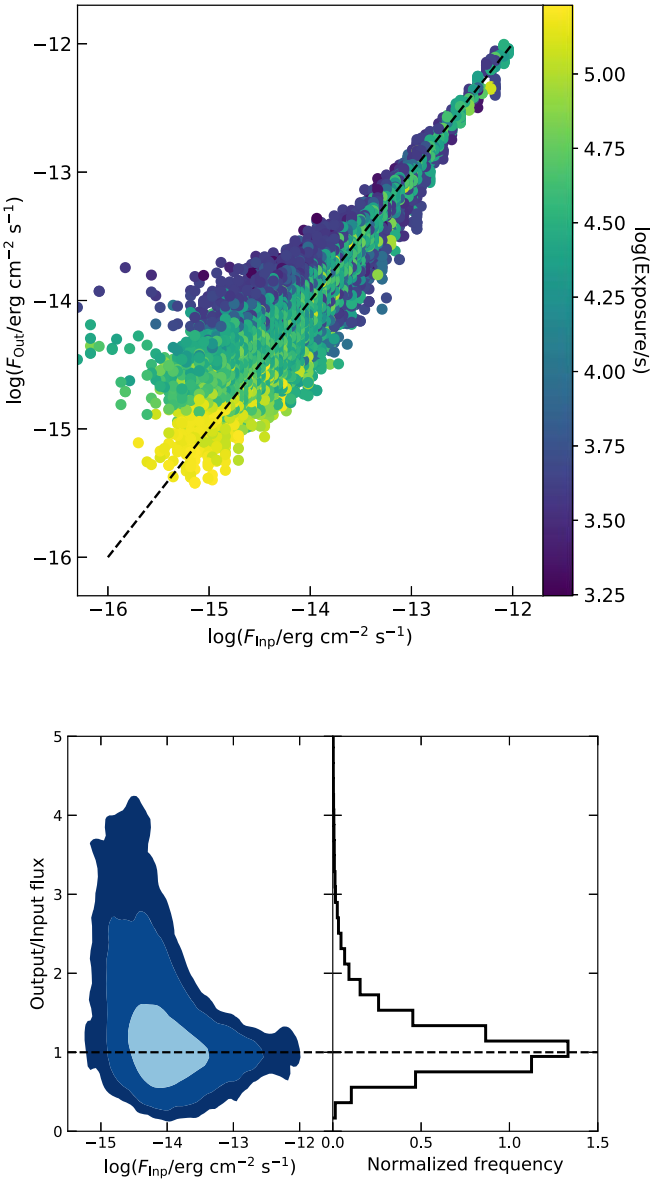

Figure 8. Top: comparison of the output flux (measured through aperture photometry) as a function of the relative input flux for sources simulated, detected, and matched to their input counterparts for a full set of 10 realizations. The dashed black line shows the 1:1 relation. The Eddington bias effect is clearly visible at fluxes $F \lesssim 10^{-14}$ erg cm^{-2} s^{-1} as an increased systematic positive spread in the output fluxes toward faint input fluxes. The points are color-coded by the logarithm of their exposure time, with deeper exposures labeled by brighter colors. Bottom: contours of the ratio between the output fluxes over the input fluxes as a function of input flux (left). The contours label 68%, 95%, and 99% of the sources in shades of blue. On the right, the same distribution shows a sharp peak around 1 (black dashed horizontal line) and the Eddington bias tail.

3.2. Completeness and Sensitivity

Using the simulations, we could test how well we measure fluxes, comparing output and input fluxes, and compute the completeness of our sample. In particular, the comparison of the output and input fluxes shows the well-known Eddington bias (Eddington 1913), for which faint sources close to the flux limit of the survey tend to be brighter than their actual flux due to positive fluctuations being more likely to be detected than negative ones. This is exemplified in the top panel of Figure 8, where the points show (detected) single sources matched to their input counterparts. The Eddington bias effect is also clearly visible in the bottom panel of Figure 8.

The ratio of the number of matched sources to the number of input ones as a function of (input) flux decreases toward fainter fluxes, reflecting the incompleteness of the survey. This ratio, rescaled by the total area of the survey, is in excellent agreement with the expected sensitivity curve obtained using an analytical calculation that includes Eddington bias (Georgakakis et al. 2008), as shown in Figure 9. To compute the expected sensitivity curve taking into account Eddington bias, we first multiplied each pixel of the background map mosaic with the exposure-averaged area of the PSF at that location, given by πr_{90}^2, so that $B^* = B \times \pi r_{90}^2$. Then we computed the minimum number of counts that, given the background value B^* in that pixel, would result in a significant detection (i.e., a probability that counts are due to a background fluctuation lower than the imposed threshold). Then we defined an array of fluxes s, and we converted it into an array of expected number of counts, given by $T = s\mathcal{C}f_{\rm PSF}\,t_{\rm Exp} + B^*$, where $\mathcal{C}$ is the ECF from flux to count rate, $f_{\rm PSF}$ is the encircled energy fraction of the PSF (0.9 in our case), and $t_{\rm Exp}$ is the exposure time. For each pixel, we ended up with an array of probabilities P(cts, T) that the minimum number of counts are observed, given the expected number of counts T. Finally, summing up all pixels at any given flux resulted in the expected sensitivity curve. The dips at high fluxes in Figure 9 are due to a handful of bright sources being undetected. Such sources mainly fall on the very edge of the mosaic and have a sufficiently large PSF that their effective surface brightness is lowered. In one case, a bright source was missed entirely because it lay very close to another (brighter) source and was detected and rejected by our code that removes duplicate detections in PSF wings. Representative values of flux limits at different levels of completeness are tabulated in Table 2.

4. Source Detection

The same detection procedure used for the simulations was applied on the real data mosaics separately for the three bands. After running `wavdetect` on each data mosaic separately, we refined the positions of each candidate source following Murray et al. (2005). Since the mosaics have a pixel scale of $1\farcs968 \times 1\farcs968$,[39] we produced a full-resolution cutout of 100 native Chandra pixels around the position of the putative source and iteratively centroided the events within r_{90}.[40] Once the coordinates were refined for the whole list of candidate sources returned by `wavdetect`, we performed aperture photometry on the full-resolution mosaic and cleaned each list for duplicates.

Since a large fraction of these sources are expected to be detected in multiple bands, a cross-match between the F, S, and H catalogs was done using r_{90} as a matching radius. The merging of the catalogs returned 6838 unique X-ray sources detected above the reliability threshold in at least one band. The average number of spurious sources detected in the simulations

[39] There could be cases in which multiple nearby sources, with a PSF smaller than the 4×4 pixel scale, were detected as a single source. Hence, we visually inspected all 562 sources in the final catalog with $r_{90} < 1\farcs96$, finding only one case of two sources blended as one due to the spatial binning. We corrected the entry of this source, adding two distinct entries at the bottom of the final catalog.

[40] In the case of sources for which r_{90} is smaller than 3″, we fixed it to 3″ to avoid the rare occurrence of small regions with zero events to centroid.

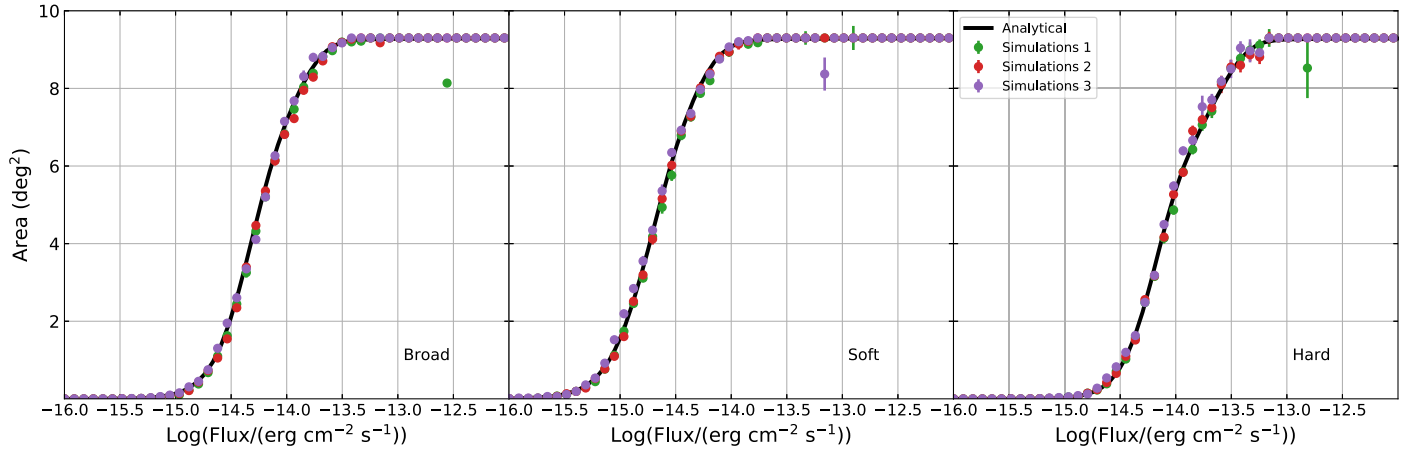

Figure 9. Sensitivity of the CDWFS for the bands employed (from left to right: broad, soft, and hard). The results from our three independent sets of simulations (each set has a different list of input sources) are shown with colored points (median of 10 simulations), with standard deviation as uncertainty. The solid black line indicates the sensitivity computed following Georgakakis et al. (2008), whose analytical computation includes the Eddington bias and expected spurious sources. The dips at bright fluxes are mostly due to bright sources being undetected due to edge effects; see the text for more details.

(58, 48.5, 52) translates into an expected spurious fraction of ∼(0.9%, 0.9%, 1.6%) for the *F*, *S*, and *H* bands, respectively.

4.1. Positional Errors

When a source was detected in more than one band, we used the coordinates of the band with the most significant detection as the final X-ray position, and we computed the positional error as $r_{50}/\sqrt{N}$ (Puccetti et al. 2009), where r_{50} was estimated from r_{90} as $r_{50} = 5/9 \times r_{90}$,[41] and N is the net counts (within r_{50}) in the band with the most significant detection. When r_{50} was smaller than a 4×4 pixel area of our mosaic, we used r_{90} instead (this was necessary for ∼2% of the sources). The distribution of the positional errors derived in this way is shown in Figure 10 and has a median value of ∼0.″8. Positional errors formally smaller that 0.″1 (occurring for 19 very bright sources) have been conservatively set to 0.″1, following Civano et al. (2016) and Puccetti et al. (2009). The cumulative distribution shows that 90% of the sources have a positional error of <1.″5 and 99% less than 2.″5, while 71% of them have a positional error smaller than 1″. These somewhat nonoptimal values (compared, for example, with the values reported by Civano et al. 2016, for the Chandra COSMOS Legacy survey, in which 85% of the sources have a positional error of <1″) could be attributed to the large fraction of observations overlapping with a significantly different roll angle, which ultimately results in a slightly larger PSF size on some parts of the field, and the lower median net counts of the CDWFS sources (15, 11, and 13 compared to 30, 20, and 22 in Chandra COSMOS Legacy in the *F*, *S*, and *H* bands, respectively). Our positional errors are consistent with the errors derived using 68% confidence level formulae as reported by Kim et al. (2007a). Hence, we consider our positional errors as 1σ uncertainties on the position of detected sources.

4.2. Counts and Fluxes

Once a unique set of coordinates was derived for each source, we reextracted aperture photometry for all bands at the same position, analogous to what was done for the simulations. We briefly recall the procedure here. Using the exposure-weighted average r_{90} to extract counts, background counts, and exposure, we computed the net counts and converted them to a count rate. The flux was computed correcting the count rate for the encircled energy fraction of the PSF within r_{90} and converted to flux using the exposure-weighted average ECF (assuming $\Gamma = 1.4$). Using a single set of coordinates for each source, the most significant detection had exactly the same aperture photometry as before, while the other two bands were adjusted and realigned with the new coordinates.

For the bands in which each source was not significantly detected, this procedure assigned a new probability of being spurious. If this new probability was higher than our imposed detection threshold, we considered the source to be detected in that band (although originally missed by `wavdetect`) and computed its count rate and flux as outlined above. If, instead, the source had a probability of being spurious higher than our adopted threshold, we computed 3σ upper limits on the net counts, count rate, and flux following Gehrels (1986).

The distributions of fluxes measured for sources significantly detected in each of the three bands are shown in Figure 11; for display purposes, the brightest source in the field, i.e., the variable star KT Boötes (*F*-band flux of $F_X \sim 3 \times 10^{-12}$ erg cm^{-2} s^{-1}), is not included.

4.3. Comparison with XBoötes

As a final step, we cross-matched our catalog with that of Kenter et al. (2005), which contains 3293 X-ray point sources detected with more than 4 counts.[42] We found that 447 out of 3293 XBoötes sources (∼14%) do not have an entry (within $1.1 \times r_{90}$) in the CDWFS catalog. Such a high number of missing sources cannot be simply explained by the spurious fraction of the XBoötes survey, expected to be around 1% (Kenter et al. 2005). The large majority (95%) of the missing XBoötes sources have ⩽6 counts in the Kenter et al. (2005) catalog. Of the 21 missing sources with seven or more counts, half of them are spread over such a large PSF area that the background is nonzero, and their significance drops. A few other sources are genuinely drowned out by the background

[41] We verified that this formula correctly approximates the increase of PSF size with off-axis angle, as shown in the Chandra Proposers' Observatory Guide.

[42] Due to the astrometric shift discussed in Section 2 and Appendix A, we shifted the position of each XBoötes source before matching it to our catalog.

Table 2
Flux Limits at Different Completeness Values

Band	Completeness										
	99%	95%	90%	80%	70%	60%	50%	40%	30%	20%	10%
F	33.3	20.6	15.7	11.0	8.26	6.62	5.45	4.51	3.71	2.96	2.14
S	13.1	7.86	5.95	4.20	3.24	2.59	2.12	1.74	1.41	1.10	0.77
H	66.1	40.5	30.7	20.4	14.1	10.6	8.39	6.91	5.70	4.58	3.35

Note. Fluxes are in units of 10^{-15} erg cm^{-2} s^{-1}. To obtain the area covered at any tabulated flux limit, the completeness must be rescaled by the total area of the field, 9.3 deg^2.

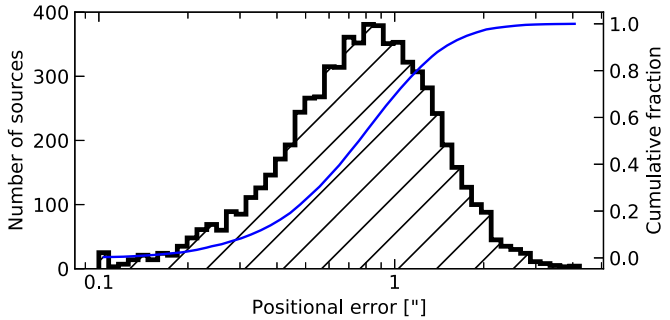

Figure 10. Distribution of the X-ray positional errors for our sample, computed following Puccetti et al. (2009). The blue line shows the cumulative histogram and implies that 90% of the sources have an uncertainty on their position lower than $1\farcs5$.

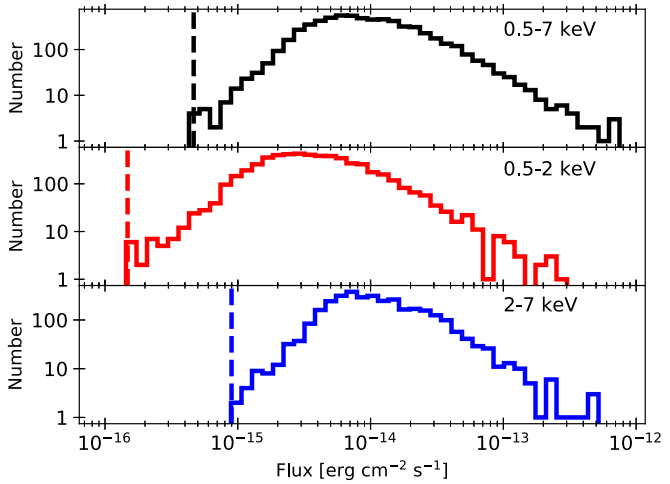

Figure 11. Distribution of the X-ray fluxes in the three bands as labeled (from top to bottom: broad, soft, and hard bands, respectively), computed with aperture photometry. In each panel, the vertical dashed line marks the faintest flux with a significant detection. We did not include upper limits for sources undetected in each band.

with deeper data. For others, there is a count mismatch; i.e., unrealistically large PSF radii are required to match the number of counts reported in the XBoötes catalog. These latter cases imply that the updated data reduction and/or different light-curve filtering may have introduced some subtle differences among the CDWFS and XBoötes data.

Table 3 shows the breakdown of the missing sources, split into sources absent from the candidate list of sources in output from `wavdetect` and those additionally missed due to our reliability cuts (i.e., detected as potential sources by `wavdetect` and later rejected). It can be seen from Table 3 that the majority of the missing sources (283/447 ∼ 63%) are already missing from the `wavdetect` output of candidates. While

Table 3
Breakdown of the Missing XBoötes Sources

		`wavdetect`	Reliability	Total
Not significant		243	151	394
Exposure	<10 ks	75	104	179
	>10 ks	168	47	215
Significant		40	13[a]	53
Exposure	<10 ks	14	4	18
	>10 ks	26	9	35
Total missing		283	164	447

Notes. The column `wavdetect` refers to XBoötes sources missing from the whole list of candidate sources in output from `wavdetect`, while the column Reliability refers to the additional missing sources excluded by our imposed probability cuts. Of the 447 missing XBoötes sources, the 53 significant ones were included in the CDWFS catalog, while the 394 that were not significant were discarded. However, an additional table is provided listing all 394 excluded XBoötes sources (see Appendix B).
[a] The very few sources missing due to reliability cuts, but then readded for being significant, are sources for which a tiny shift between the candidate position returned by `wavdetect` and the actual XBoötes position is enough to move the source above/below the threshold.

two-thirds of the total area of the field is covered by additional data compared to the original XBoötes survey, one-third of the area (∼3 deg^2) comprises the very same data. A rough distinction between sources lying on the same XBoötes data and those falling where new observations have been done is obtained in Table 3 by splitting the missing sources by exposure: sources with $t_{\rm Exp} < 10$ ks lie mostly over the original XBoötes edge of the field.

While Table 3 reveals that the sources missed by `wavdetect` are homogeneously scattered across the field regardless of exposure time, the reasons for missing sources in areas of different exposure are likely different. On one hand, when the exposure time is increased by coadding observations, the Eddington bias effect becomes less significant, source variability can play a role, and genuinely spurious sources are less likely to be detected again. Among these factors, the first one is likely the most effective in this case: our simulations show that ∼16% of simulated sources with $t_{\rm Exp} < 8$ ks are detected with an output flux more than twice the input one due to Eddington bias. The effect drastically reduces to ∼3% for sources with $t_{\rm Exp} > 40$ ks. A possible additional role could be played by the degrading sensitivity of Chandra with time, resulting in diluting the genuine signal of faint sources with the increasing exposure (and hence background).

On the other hand, XBoötes sources missing from `wavdetect` output on the very same XBoötes data require a more careful treatment and a different explanation. As

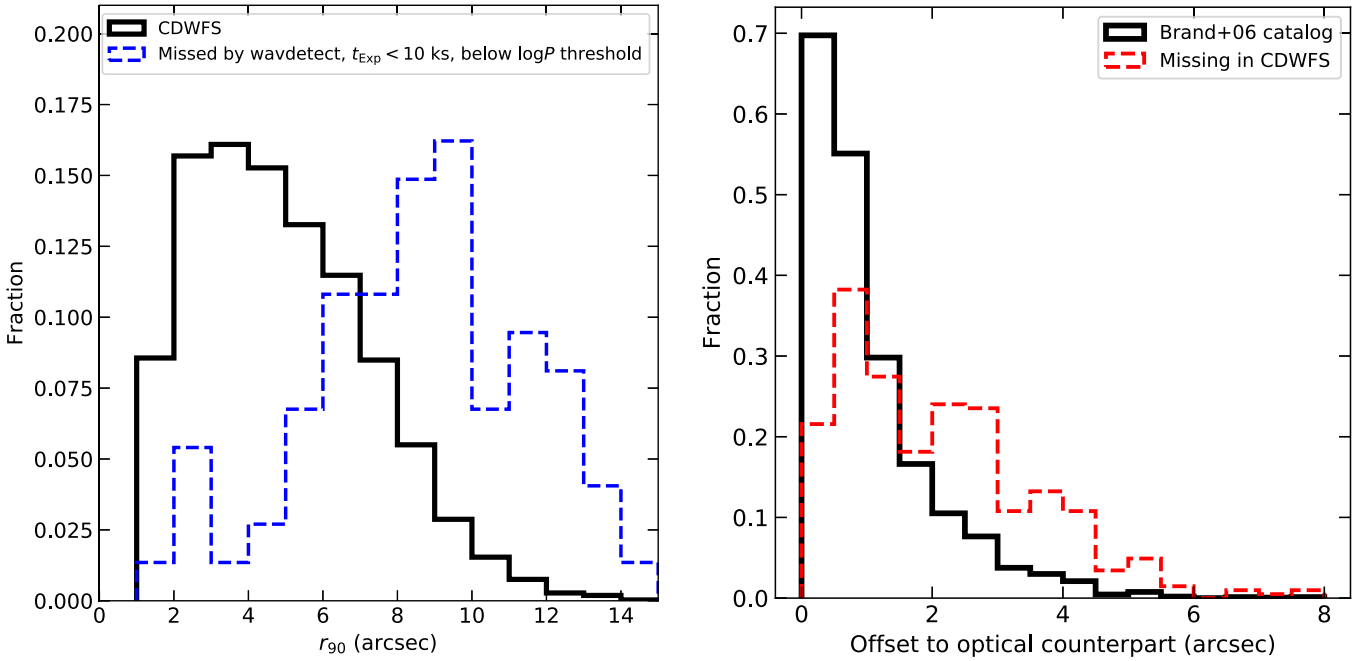

Figure 12. Left: normalized distribution of the average r_{90} for the full CDWFS sample (solid black histogram) and the subset of XBoötes sources missing from the output list of candidate sources having exposure <10 ks (dashed blue histogram). The two distributions are clearly different and suggest that `wavdetect` does not detect such sources due to the additional PSF size information, different from what was done in Murray et al. (2005). Right: normalized distribution of the offset between XBoötes sources and their optical counterparts as measured by Brand et al. (2006). The missing sources (red dashed histogram) are, on average, more offset from their best (i.e., higher rank) optical counterparts than the full catalog, shown by the solid black histogram. This may indicate that the positional error of the missing sources is larger than average due to their low counts and large off-axis angles.

discussed in Section 3, `wavdetect` was run on the whole field mosaic, with additional inputs such as the exposure map and PSF mosaics.[43] Murray et al. (2005) and Kenter et al. (2005) did not mention if any additional information was fed to `wavdetect`, but it is likely they did not use exposure or PSF maps when detecting sources over each of the 126 XBoötes observations. In the left panel of Figure 12 can be seen that our inclusion of the PSF information is very likely playing a role. The median r_{90} of the sources lying on the low-exposure part of the field and missed by `wavdetect` is almost twice the median r_{90} of the CDWFS catalog.[44] Smoothing the low counts of such sources on a large PSF area likely dilutes their contrast with the background and lowers their significance. This emphasizes a caveat regarding using a simple circular area of radius r_{90} to detect sources and extract aperture photometry. The sampling of the PSF is indeed not homogeneous, and counts (especially in a low-exposure, low-counts regime) will generally not distribute uniformly across the circular area. A more rigorous approach would require taking into account the actual shape and substructure of the PSF when detecting sources and extracting aperture photometry, which is outside the scope of this work.

The fact that sources missed by `wavdetect` have generally larger off-axis angles is corroborated by the distribution of offsets between XBoötes sources and their optical NDWFS counterparts as defined by Brand et al. (2006). In the right panel of Figure 12, it is clear that sources missing in CDWFS show larger-than-average offsets to their matched optical counterparts, likely a combination of large positional errors (deriving from large PSF sizes and low X-ray counts) and faint optical counterparts. Indeed, considering the whole Brand et al. (2006) catalog of XBoötes optical counterparts, we find that ∼62% have an entry in the AGN and Galaxy Evolution Survey (AGES) optical spectroscopic catalog of Kochanek et al. (2012). However, when considering the subset of 447 XBoötes sources missing from CDWFS, only ∼38% have an entry in the AGES catalog. Once again, this confirms that these sources are likely very faint and with low significance.

Thus, unsurprisingly, even if all 447 sources would have been picked up by `wavdetect`, ∼88% of them would have been rejected by our imposed thresholds. The remainder of the sources (∼12%, 53) that satisfy our reliability thresholds have been added to our catalog. For the newly added sources, aperture photometry was computed for each band at the position of the source in the Kenter et al. (2005) catalog, extracting counts from the full-resolution mosaic, analogous to what was done for the other sources. As can be seen in Table 3, the majority of these significant sources (40) were genuinely missed by `wavdetect`, while a few of them were missed due to reliability cuts. These latter sources are few, rare cases in which the position returned by `wavdetect` is slightly offset with respect to the position in the Kenter et al. (2005) catalog. This tiny offset (often around one native Chandra pixel) is enough to make the source significance fluctuate across the thresholds.

4.4. Summary of Source Detection

After detecting sources independently in the *F*, *S*, and *H* bands, merging the three catalogs together into a list of 6838

[43] The scales over which `wavdetect` was run are also slightly different compared to XBoötes; we did not include the largest 8 pixel scale (corresponding to $8 \times 1\farcs968 = 15\farcs74$) mentioned by Kenter et al. (2005), but we verified that the difference cannot be explained by adding this scale.

[44] The effect is also seen with the total sample of sources missed by `wavdetect`, although with a lower significance.

Table 4
Breakdown of the Number of Sources Detected in Each Combination of Bands

Combination	Number	Fraction
FSH	2498	36.3%
FS	2354	34.2%
FH	720	10.4%
SH	0	0%
F	842	12.2%
S	386	5.6%
H	91	1.3%
Total *F*	6414	93%
Total *S*	5238	76%
Total *H*	3309	48%

sources, and adding 53 significant XBoötes sources, the final number of unique, X-ray point sources in our catalog is 6891.

Estimating the final spurious fraction of the CDWFS catalog is not trivial, since our simulations treat each band independently (we recall that we expect, on average, 58, 48.5, and 52 spurious sources from simulations in the *F*, *S*, and *H* bands, respectively) and we added some sources from a previously published catalog. In a best-case scenario in which all spurious sources of the *F* band are made up by the spurious sources of the *S* and *H* bands, which are instead detected independently, and none of the added XBoötes sources is spurious, we would end up with an estimated spurious fraction of $100.5/6891 = 1.5\%$. In a worst-case scenario in which the spurious sources in the *F*, *S*, and *H* bands are all different sources, and 1% of the added XBoötes sources are also spurious, we would end up with a spurious fraction of $159/6891 = 2.3\%$. We estimated the most likely true spurious fraction by computing how many *F*-band spurious sources could also be detected in the *S* and *H* bands by splitting the *F*-band counts into the *S* and *H* bands assuming $\Gamma = 1.4$ and through Poisson statistics. On average, 14% and 41% of the *F*-band spurious sources would satisfy our reliability thresholds in the *S* and *H* bands, respectively. Furthermore, we believe the 53 XBoötes sources that satisfy our reliability thresholds to be real. Hence, the total number of spurious sources in the final catalog is expected to be $\sim 127/6891 = 1.8\%$.

Along with the list of the excluded 394 XBoötes sources ($447 - 53$) that do not satisfy our thresholds, we also release the full electronic CDWFS catalog. An extract of the first 10 sources of both catalogs can be found in Appendix B (Table B1 and B2, respectively), while the full lists are available online as electronic catalogs.

The final detailed breakdown of the number of X-ray sources detected in each combination of the three bands is reported in Table 4.

5. Number Counts

A typical check on the quality of an X-ray-selected catalog is to derive the number counts distribution (i.e., the number of sources per unit flux and area) and the integral of that distribution (the log*N*–log*S* curve). Of course, different biases have to be taken into account to derive accurate number counts. For example, the observed fluxes, measured through aperture photometry, are subject to Eddington bias (as also shown by our simulations; see Figure 8). Moreover, the sensitivity of the survey has to be taken into account when correcting for missing sources at the faintest fluxes.

In general, number counts can be derived by simply correcting the flux histogram for the incompleteness of the survey and then integrating the number of sources per square degree and flux bin to recover the log*N*–log*S*. This first method, which we will refer to as "standard," is straightforward but has the disadvantage of ignoring Eddington bias and the fraction of spurious sources.

A second method is more complicated (we will refer to it as "nonstandard") but allows us to correct for Eddington bias and naturally take into account spurious sources. This method, extensively described in Georgakakis et al. (2008), considers all of the sources significantly detected in a given band. Each source is detected with $\mathcal{N}$ total counts and B expected background counts within an exposure time $t_{\rm Exp}$. To take into account the uncertainty on each measured flux, a flux probability density function (PDF) can be defined,

$$P(\mathcal{N}, T) = \frac{T^{\mathcal{N}} e^{-T}}{\mathcal{N}!}, \tag{2}$$

where this function gives the probability of observing $\mathcal{N}$ counts given T, where T can be explicitly written (similar to what is done in Section 3.2) as a function of flux s as $T(s) = s\mathcal{C}f_{\rm PSF}\,t_{\rm Exp} + B$, where $\mathcal{C}$ is the ECF from flux to count rate, and $f_{\rm PSF}$ is the encircled energy fraction of the PSF (0.9 in our case). As discussed by Georgakakis et al. (2008), if a source is detected with $\mathcal{N}$ counts, its flux PDF must also be weighted by an underlying dN/dS. This factor is needed to account for the fact that there are more faint sources that could fluctuate up to higher fluxes than bright sources that fluctuate down, effectively including Eddington bias in the calculation.

Since the exact shape of the underlying dN/dS is what we are looking for, we applied a maximum-likelihood method to obtain the best-fit dN/dS. First, we defined a range of fluxes s and computed this quantity for each source:

$$P_i = \frac{\int P(\mathcal{N}, T(s)) \frac{dN}{ds} ds}{\int A(s) \frac{dN}{ds} ds}, \tag{3}$$

where $A(s)$ is the sensitivity curve as derived in Section 3.2. Then, the likelihood of the whole set of sources is given by $\mathcal{L} = \prod_i P_i = \sum_i \log P_i$. This procedure returns the best-fit parameters of the dN/dS, which can be used to compute the observed number counts. Since the PDFs are defined over a large range of fluxes, extending fainter than the nominal flux limit of the survey, this method also allows one to extrapolate to fluxes that are formally inaccessible to the survey.

5.1. Simulated Number Counts

We first explored whether we could accurately recover the input log*N*–log*S* of the simulations.

We applied both methods and compared their robustness in recovering the input log*N*–log*S* in our simulations. As shown in Figure 13, both methods are generally able to recover the input log*N*–log*S*. As expected, the nonstandard method (the set of colder colors in Figure 13) better recovers the input shape. It is worth noting that the lower panels of Figure 13 show the ratio between output/input log*N*–log*S* where the input log*N*–log*S* corresponds to the analytical shape of the curve, not the actual Poissonian realization effectively used for the different sets of simulations. The spread of the measured number counts at

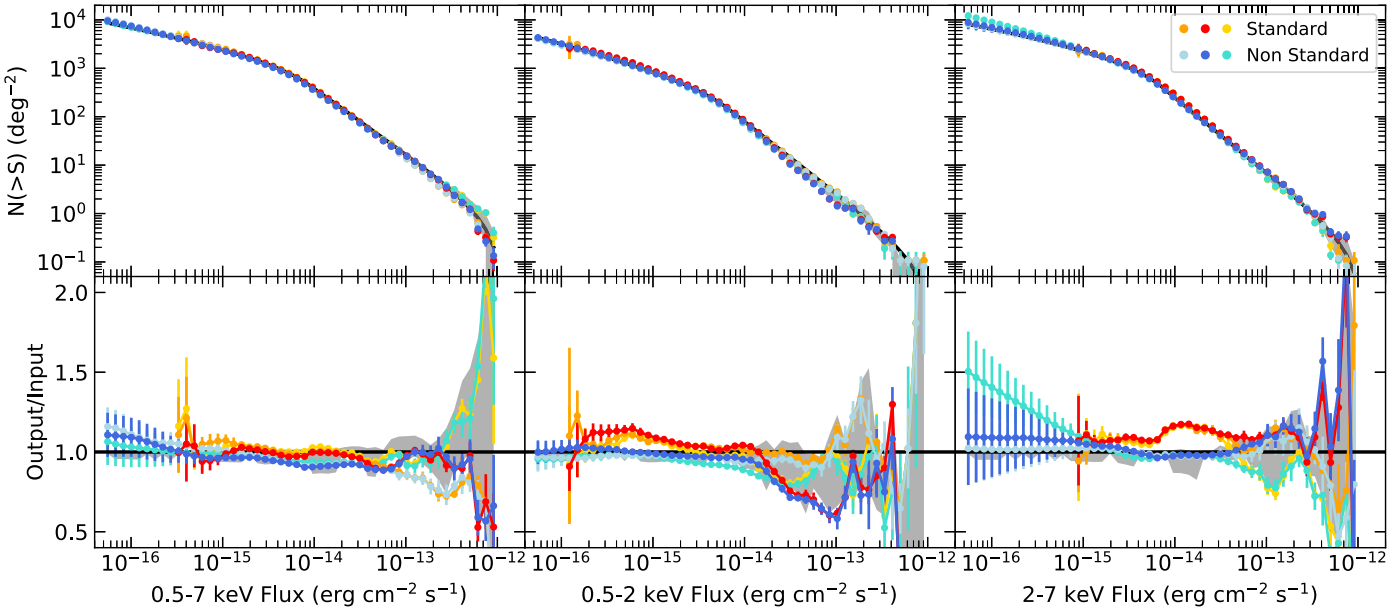

Figure 13. Performance of our measurement of the log$N$–log$S$ on simulations. From left to right, we show the broad, soft, and hard bands. The upper panels show the recovered log$N$–log$S$ with points and the input one with a solid black line, while the lower panels show the ratio between the points and the input log$N$–log$S$. The sets of warm and cold colors refer to the standard and nonstandard methods, respectively, while in each set, the color specifies a set of 10 simulations.

bright fluxes is due to the Poisson fluctuations introduced by this process, depicted using gray shading in Figure 13.

As can be seen in Figure 13, in the hard band, one simulation set overshoots the faint end of the input log$N$–log$S$ by a factor of $\lesssim$1.5. However, this happens only in the hard band, in one set out of three simulations, and only when extrapolating to fluxes below the flux limit (which is depicted in Figure 13 by the warm colors, as the standard method extends over the range of actual fluxes of the detected sources). In summary, we are confident that both methods fairly recover the underlying distribution of the number counts, and the nonstandard method is more accurate and reliable over the range of fluxes covered by our sources.

5.2. Number Counts and Resolved Fraction of the CXB

Motivated by the previous analysis, we applied both methods to our X-ray catalog to derive robust number counts, exploiting the large number of sources detected in each band. As reported in the second column of Table 5, all sources significantly detected in each band (excluding the brightest source in the field, which, as stated previously, is a star) were used in the following computation. The differential number counts were fit with a broken power law of the form

$$dN/dS = \begin{cases} K\,(S_x/S_{\rm ref})^{\beta_1}, & S_x \leqslant S_b \\ K\,(S_b/S_{\rm ref})^{\beta_1-\beta_2}(S_x/S_{\rm ref})^{\beta_2}, & S_x > S_b \end{cases}, \quad (4)$$

where $S_{\rm ref} = 10^{-14}$ erg cm^{-2} s^{-1} and S_b is the break flux; the results are shown in Table 5. The uncertainties were estimated through bootstrapping. We note that in this analysis, we did not separate AGNs from galaxies and stars. However, we expect galaxies to have a negligible impact on the number counts at the relatively bright fluxes probed here, with stars even less significant (see Lehmer et al. 2012). Having computed the differential number counts, we integrated them to obtain log$N$–log$S$, which is shown in Figure 14 for the nonstandard method. Note that the results using the standard method are fully consistent with those in the figure apart from some fluctuations due to the different treatment of Eddington bias.

Table 5
Best-fit Parameters for the Differential Number Counts for the Boötes Field

Band	Sources	K_{14}	S_b	β_1	β_2
F	6413	335 ± 2	22 ± 3	-1.78 ± 0.03	-2.59 ± 0.08
S	5237	141 ± 2	8.1 ± 1.2	-1.68 ± 0.03	-2.56 ± 0.09
H	3308	274 ± 1	19 ± 5	-2.03 ± 0.06	-2.76 ± 0.10

Note. The second column gives the number of sources used to derive the number counts. Here K_{14} is the normalization in units of 10^{14} deg^{-2} (erg cm^{-2} s^{-1})$^{-1}$, while the break flux S_b is in units of 10^{-15} erg cm^{-2} s^{-1}.

Figure 14 also shows the number counts from other Chandra surveys.[45] Since CDWFS updates the previous XBoötes survey, it is particularly informative to consider the best-fit log$N$–log$S$ from Kenter et al. (2005) in the soft and hard bands (solid green lines in Figure 14). In the soft band, Kenter et al. (2005) fit their number counts with a broken power law; our results are consistent with these results, and we can better constrain the parameters of the fit. On the other hand, Kenter et al. (2005) fit the hard number counts with a single power law and obtained a significantly steeper slope, while the results we obtain for CDWFS are in much better agreement with other Chandra surveys, at least at the bright end of the distribution. In particular, the faint end of the hard-band log$N$–log$S$ appears to be steeper than the other measurements, even before extrapolating. This higher density is also found with log$N$–log$S$ computed using the standard method. Wang et al. (2004) also noted this higher density and attributed it to an overdensity of faint hard X-ray sources in the deepest region of the field (i.e., the LaLa survey; Wang et al. 2004).

The best-fit parameters of the differential number counts can also be used to infer the resolved fraction of the CXB; this is

[45] When the energy bands did not exactly match the ones we employed, we converted the fluxes assuming $\Gamma = 1.4$.

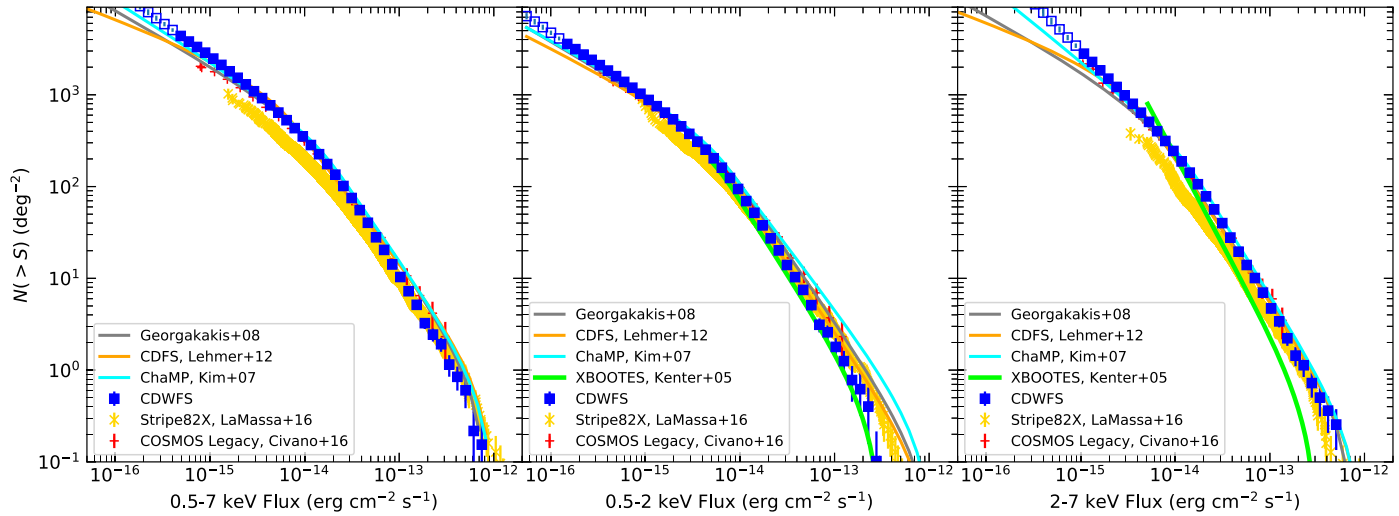

Figure 14. Measurement of the log$N$–log$S$ on data. From left to right, we show the broad, soft, and hard bands. Only the log$N$–log$S$ obtained from the nonstandard method are shown with blue squares, with open symbols when extrapolating below the flux limit of the survey. The results are fully consistent with the log$N$–log$S$ obtained with the standard method (apart from the missing correction for Eddington bias), not shown here for clarity. As a comparison, the best-fit log$N$–log$S$ presented in Georgakakis et al. (2008) for a collection of Chandra surveys, Lehmer et al. (2012) for CDFS, and Kim et al. (2007a) for the ChaMP survey are shown with colored lines. In the soft- and hard-band panels, the best-fit log$N$–log$S$ relations from XBoötes (Kenter et al. 2005) are shown as solid green lines. While our results are fully consistent with the XBoötes best-fit log$N$–log$S$ in the soft band, the hard-band parameters reported by Kenter et al. (2005) were for a single power law (i.e., not a broken power law) and have large associated uncertainties. Finally, the measured log$N$–log$S$ from Chandra COSMOS Legacy (Civano et al. 2016) and Stripe82X (LaMassa et al. 2016) are shown with red and yellow symbols, respectively. The Boötes field log$N$–log$S$ is broadly consistent with other fields in the broad and soft bands, while in the hard band, there is a significant overshooting at faint fluxes, presumably due to the overdensity of sources in the deepest areas of the field, as already noted by Wang et al. (2004).

trivially done by computing the integral

$$\int_{S_{\rm min}}^{S_{\rm max}} \frac{dN}{dS} S dS, \tag{5}$$

where $S_{\rm min}$ and $S_{\rm max}$ are the minimum and maximum flux of the detected sources. The result of this integral gives the total X-ray flux per square degree resolved into single sources. Thus, the fraction of resolved CXB is obtained by comparing the resolved flux to the total CXB intensity in a given energy band. Converting the values reported by Hickox & Markevitch (2006) to match our energy bands assuming $\Gamma = 1.4$, we obtained a resolved fraction of $65.0\% \pm 12.8\%$ and $81.0\% \pm 11.5\%$ for the soft and hard bands, respectively. The uncertainties were estimated assuming a normal PDF for the parameters of the dN/dS and solving the integral 5000 times, each time randomly picking the parameters according to their PDFs. The uncertainty on the total intensity of the CXB as reported by Hickox & Markevitch (2006) was propagated to obtain the error on the resolved fraction. Since in this paper, we detected only point sources, the resolved flux does not take into account the contribution from extended sources (such as galaxy clusters or groups), which is expected to be larger in the soft band. The resolved fraction of the CXB is consistent within the uncertainties with that reported by Kim et al. (2007b) for the ChaMP survey in both the S and H bands, at comparable depth and total area with CDWFS; also, in the H band, with that reported by Hickox & Markevitch (2006).

6. Optical–IR Counterparts

The Boötes field has rich multiwavelength coverage from the radio to the X-rays, which we briefly summarize here. In the radio, many frequencies are covered, including LOFAR LBA (50 MHz; van Weeren et al. 2014) and HBA (150 MHz; Retana-Montenegro et al. 2018), as well as the GMRT (153 MHz; Williams et al. 2013), Very Large Array (325 MHz; Coppejans et al. 2015), and 1.4 GHz WSRT (de Vries et al. 2002). Far-IR data are available from the Herschel Multi-tiered Extragalactic Survey (HerMES; Oliver et al. 2012), providing data from both SPIRE at 250, 350, and 500 μm and PACS at 110 and 170 μm.

Mid-IR (MIR) coverage is available from both the Spitzer MIPS AGN and Galaxy Evolution Survey (MAGES; Jannuzi et al. 2010) and the Spitzer Deep Wide-field survey (SDWFS; Ashby et al. 2009; Kozłowski et al. 2010, 2016), complementing the earlier Spitzer IRAC Shallow Survey (Eisenhardt et al. 2004) in the four IRAC channels. Near-IR data in the J, H, and K_s bands are available from the NEWFIRM Infrared Boötes Imaging Survey (IBIS; Gonzalez et al. 2010), and Y-band data are available from LBT (Bian et al. 2013). Optical photometry is provided by NDWFS in the B_W, R, and I bands (Jannuzi & Dey 1999), LBT in the $U_{\rm spec}$ band (Bian et al. 2013), and zBoötes in the z band (Cool 2007). Multiband photometry for I-band detected sources is also available (Brown et al. 2007). In addition, optical spectroscopy is available from AGES (Kochanek et al. 2012). The UV coverage is provided by the Galaxy Evolution Explorer, and extensive X-ray coverage from Chandra is available from our work (CDWFS) and the previous XBoötes survey (Murray et al. 2005).

Following a standard approach adopted in X-ray surveys, we matched our X-ray catalog to optical and MIR data adopting the maximum-likelihood ratio technique (e.g., Brusa et al. 2005, 2007, 2010; Marchesi et al. 2016). In particular, we matched with the full I-band NDWFS (3σ depth of 22.9 Vega magnitudes) and [3.6]-selected SDWFS (5σ depth of 19.77 Vega magnitudes) catalogs, whose spatial coverages are shown

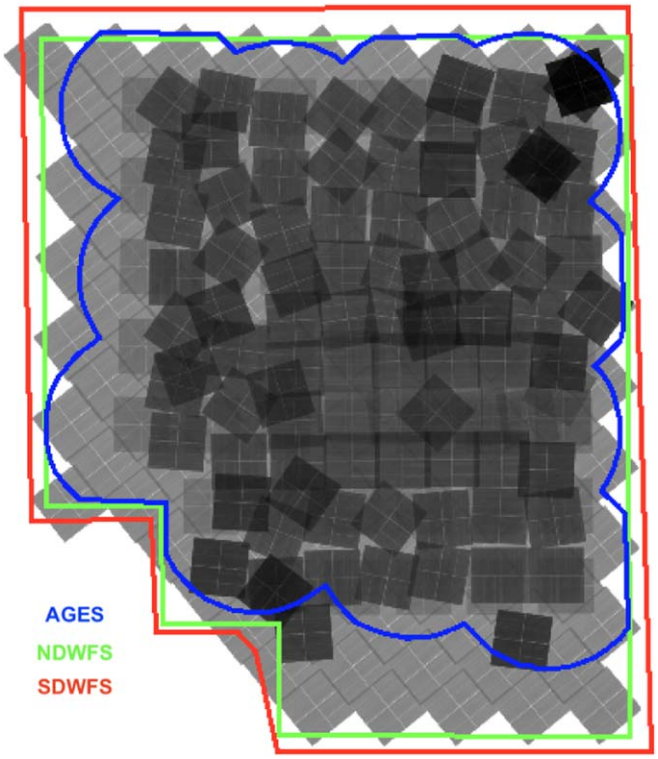

Figure 15. Multiwavelength coverage of the Boötes field considered in this work. The green region indicates the photometric coverage provided by the optical NDWFS (Jannuzi & Dey 1999), while the red one indicates the MIR SDWFS coverage (Ashby et al. 2009). Optical spectroscopy is provided by the AGES survey (Kochanek et al. 2012) and is shown in blue.

in Figure 15. We used NWAY (Salvato et al. 2018) to simultaneously match our X-ray catalog to the *I*- and [3.6]-band catalogs.

Each X-ray source in our catalog was associated with its most likely optical/IR counterpart, taking into account both the distance and the magnitude of the candidate counterpart. We considered all counterparts within 10″ of each CDWFS source and used a much stricter radius of 1″ to build the magnitude histogram of the true counterparts, as done, e.g., by Marchesi et al. (2016). While we used the computed positional error of our X-ray sources, a positional error of 0.″1 for the *I*-band catalog and 0.″5 for the [3.6]-band catalog were assumed.

The matched catalog returned by NWAY was cleaned, retaining only the most likely (if any) counterparts (i.e., those with `match_flag=1`). The left panel of Figure 16 shows the magnitude distributions of multiwavelength counterparts and their distances from our X-ray sources. The large majority (∼90%) of the counterparts are matched within 2″. Each X-ray source has a probability of being associated with its correct counterpart (the parameter `p_any`), and we estimated (by randomly shuffling the X-ray catalog and rematching it with the same maximum-likelihood ratio procedure) that a cut of `p_any` > 0.29 is required to ensure fewer than 10% spurious associations.[46] Out of 6891 X-ray sources, 6843 (5852) have at least one counterpart in the *I*- and/or [3.6]-band catalogs with `p_any` >0 (`p_any` > 0.29).

[46] To have fewer than (5%, 3%, 1%) spurious associations, `p_any` cuts of (0.68, 0.85, 0.96) should be used.

6.1. Redshifts and X-Ray-to-optical Properties

To obtain spectroscopic redshifts, we matched the CDWFS catalog with the AGES catalog (Kochanek et al. 2012) using the NDWFS *I*-band coordinates (or the SDWFS ones, for the 810 sources with IR-only counterparts) and adopting a matching radius of 0.″5. We shifted the whole AGES catalog in order to correct its astrometry with respect to Gaia (see Appendix A). In total, we had 2346 valid spectroscopic redshifts. Then, we exploited the recent release of hybrid photometric redshifts (template + machine learning; see Duncan et al. 2018a, 2018b) for the upcoming data release of the LOFAR Two-meter Sky Survey Deep Fields (Duncan et al. 2020, submitted). Analogous to that done for the spectroscopic redshifts, we matched our CDWFS sources with a matching radius of 0.″5 and chose the closest counterpart when multiple *I*-band entries were found within this distance. We ended up with a total of 6447 photometric redshifts. The overall quality of the photometric redshifts compared to the spectroscopic ones is shown in Figure 16, and it is generally very good. A handful of outliers show a photometric redshift higher than 6 but are all actually associated with much lower spectroscopic redshifts. We thus suggest caution when focusing on the 30 CDWFS sources with $z_{\rm Phot} \gtrsim 6$. The normalized median absolute deviation, $\sigma_{\rm NMAD} = 1.48 \times {\rm median}(|z_{\rm ph} - z_{\rm sp}|/(1 + z_{\rm sp}))$, is 0.054, while the fraction of outliers, defined as the fraction of sources where $|z_{\rm ph} - z_{\rm sp}|/(1 + z_{\rm sp}) > 0.15$, is 13.23%. These already excellent values and likely will soon be further improved by the upcoming Subaru HSC data coverage of the Boötes field. Table 6 summarizes the number of counterparts and redshifts for the whole X-ray catalog with `p_any` > 0 and the subset for which `p_any` > 0.29.

6.2. HR and Obscuration

Once the redshift of a given X-ray source is known, a rest-frame luminosity can be computed from the observed flux. Although very penetrating, X-rays suffer an absorption bias depending on the amount of gas column density along the line of sight (usually denoted with $N_{\rm H}$). This absorption effect is band-dependent and mostly affects soft X-rays. To derive statistically reliable absorption-corrected rest-frame luminosities, we first estimated the gas column density $N_{\rm H}$ for any given source. We used a standard method, which estimates the column density using the combination of the HR (defined as HR = (H−S)/(H+S), where H and S are the hard and soft counts, respectively) and the redshift information. The HR was computed for each X-ray source using the Bayesian estimator for hardness ratio (BEHR; Park et al. 2006) and taking into account the slightly larger area from which the hard counts have been extracted during the aperture photometry step due to the larger PSF size in the *H* band.

The HR encodes the observed spectral shape of the source; since the absorption bias is band-dependent, the redshift has to be known to properly estimate the intrinsic column density at the location of the source. We therefore created a grid of theoretical curves of HR as a function of redshift for a large range of column density using XSPEC (Arnaud 1996) and a simple power law with photon index $\Gamma = 1.8$, consistent with the average, absorption-corrected value of the whole AGN population (e.g., Ricci et al. 2017). We modified the assumed power law to account for absorption by a fixed Galactic column density $N_{\rm H,Gal} = 1.04 \times 10^{20}\,{\rm cm}^{-2}$ (Kalberla et al. 2005),

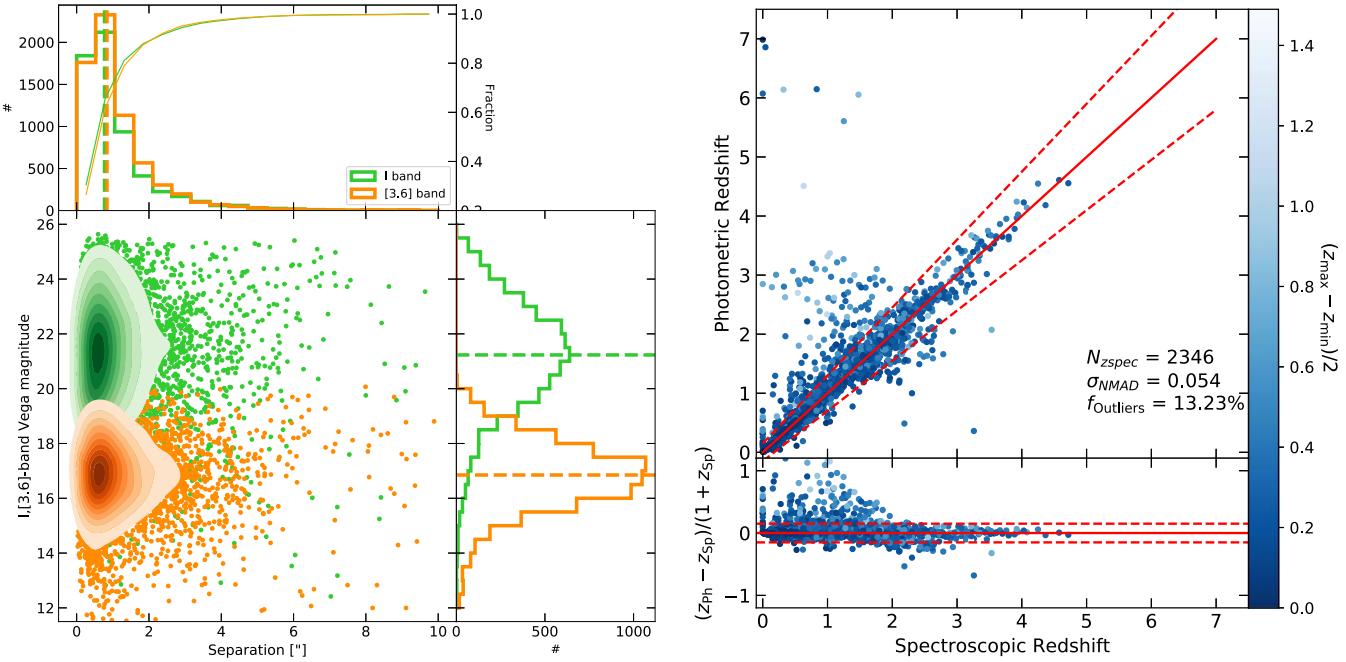

Figure 16. In the left panel, the middle plot shows the separation–magnitude plane for all CDWFS sources with an *I*- and/or [3.6]-band counterpart, shown as green and orange dots, respectively. The overlaid contours qualitatively show the density gradient of sources in the plane. The top plot shows the separation distributions. The medians of the distributions are shown by vertical dashed lines and are both $\sim 0\farcs8$. The cumulative distributions are also given as thin lines and show that 90% of the counterparts are matched within $2''$. The right plot shows the magnitude distributions for the two samples, with the medians of the distributions given as dashed lines. Right: comparison between photometric and spectroscopic redshifts for the 2346 sources with a valid spectroscopic redshift entry. Points are color-coded by their approximate uncertainty. The solid red line marks the 1:1 relation, while the dashed red lines limit the region of $\Delta z/(1 + z_{sp}) = \pm 0.15$. Sources outside this region are marked as outliers and represent $\sim$13% of the total. This figure highlights the very good agreement between photometric and spectroscopic redshifts in the Boötes field.

Table 6
Results of the Multiwavelength Match of the CDWFS Catalog with the NDWFS and SDWFS Catalogs

	p_any > 0	p_any > 0.29
X-ray sources	6891	5852
Counterparts in at least one band	6843	5852
Counterparts in both bands	5802	5393
Available redshifts	6449	5661
Best redshift spectroscopic	2346	2287
Best redshift photometric	4103	3374

estimated approximately at the center of the Boötes field, and an additional amount of column density in the range $\log(N_H/\mathrm{cm}^{-2}) = [20, 25]$ with a step of 0.02 dex.[47]

Once the correlated parameters HR and z were known for a given source, the closest N_H-dependent theoretical curve in our grid was used to estimate the column density that, for a typical power law of $\Gamma = 1.8$ at redshift z, resulted in the observed HR (and, ultimately, the observed *S*- and *H*-band counts).

It is worth stressing that the spectral shape of a local heavily obscured AGN is much more complex than what is defined by a simple obscured power law. First, the assumed simple model does not include the effect of Compton scattering, which becomes important at the highest column densities, close to the Compton-thick threshold (i.e., $N_H \gtrsim 10^{24}\,\mathrm{cm}^{-2}$); ignoring it leads to an underestimation of the intrinsic luminosity for such highly obscured AGNs (e.g., Li et al. 2019). Moreover, the possible presence of a reflection component would harden the spectrum, resulting in an overestimation of the obscuration (e.g., Wilkes et al. 2013). In addition, prominent soft emission, likely arising from photons that have scattered off clouds on a scale much larger than the nuclear one (where most of the obscuring material lies), dominates the soft X-ray spectrum of heavily obscured AGNs at $E \lesssim 2$–3 keV (Bianchi & Guainazzi 2007; Ricci et al. 2017). This implies that, for high column densities approaching the Compton-thick level and for low-to-intermediate redshifts, the HR estimated from a more realistic model can be much softer than what would be expected from a simple obscured power law. However, if we try to incorporate a more physical model when creating a grid of theoretical HR(z) tracks, many tracks end up crossing each other, invalidating our method of using the HR–z plane to uniquely estimate individual source properties. The effect of such a simplification on estimates of column density is that a fraction of AGNs appearing as unobscured and faint will, in reality, be obscured and intrinsically more luminous (Lambrides et al. 2020). A careful assessment of the obscuration state of our sample is outside the scope of the present paper and requires a combination of multiwavelength diagnostics, e.g., using rest-frame MIR luminosities and X-ray spectral analysis, to disentangle genuine, faint, and unobscured AGNs from luminous obscured ones.

The HR–z plane, together with the relative redshift and HR distributions of our sample, is shown in the left panel of Figure 17. As can be seen from the top plot of this panel, $\sim$90% of our sample lies within $z < 3$. The HR distribution of

[47] It should be noted that theoretical HR(z) functions were obtained with model fluxes, which were then converted to count rates using the appropriate exposure-weighted ECF on a source-by-source basis. Here we are implicitly ignoring the difference in exposure time between the *S* and *H* bands so that an HR computed with count rates corresponds to one computed with observed counts. This simplification is justified because 95% of our sample has an H-to-S exposure ratio in the range 0.95–1.15.

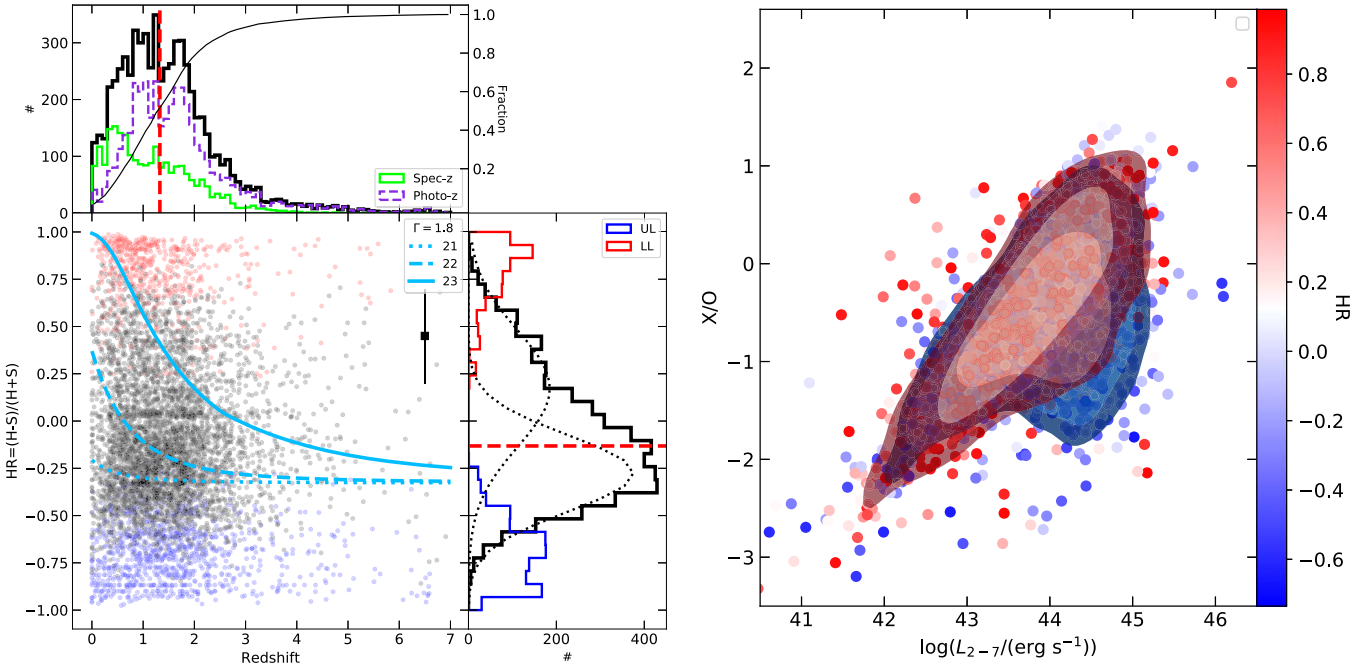

Figure 17. In the left panel, the middle plot shows the HR–z plane for all CDWFS sources with a redshift (i.e., 6465). The constrained HRs (i.e., the ones that do not reach the lower or upper allowed values within their 1σ uncertainties) are shown as black points, while upper and lower limits are shown with blue and red points, respectively. The median uncertainty on the HR for the constrained sample is shown as the black point on the right. The cyan tracks show three different HR(z) functions for $\log(N_{\rm H}/{\rm cm}^{-2}) = 21$, 22, and 23 in dotted, dashed, and solid lines, respectively. The top plot shows the redshift distribution of the sample, split into photometric (dashed violet histogram) and spectroscopic (solid green histogram). The median of the distribution is shown by a red vertical dashed line. The cumulative distribution is also shown as a thin black line. The right plot shows the HR distribution for the three samples (constrained in solid black, upper/lower limits in solid blue/red), with the median of the distribution given as a dashed red line. Also shown in dotted lines is the two-Gaussian decomposition of the black histogram. Right: X/O as a function of hard-band luminosity. Sources are color-coded by their HRs, and density contours are overlaid (red contours for 68%, 90%, and 99% of sources with HR > 0.2 and blue contours for the same fraction of sources with HR < 0). Despite large scatter due to the uncertainties on each single HR, softer sources (blue points and contours) are more spread out to lower X/Os at $L_x > 10^{43}$ erg s^{-1}, as expected for unobscured AGNs.

the whole sample, shown in the right plot, demonstrates that the median HR of the whole (HR-constrained) sample ($\overline{\rm HR} = -0.16$) is similar to the expected HR for an unobscured power law with photon index $\Gamma = 1.8$ but shifted to a harder (i.e., larger) HR. Indeed, the whole HR distribution looks asymmetric and is well fit by a double Gaussian function (e.g., Civano et al. 2016), with (μ, σ) = (0.22, 0.29) and (−0.27, 0.21) representing a mix of the unobscured and obscured populations of AGNs.

Since the early stages of X-ray surveys, AGNs have been known to occupy a well-defined region of the X-ray and optical flux parameter space. In particular, the ratio between the X-ray and optical flux, defined as X-ray–to–optical flux ratio (X/O) $= \log f_x + m/2.5 + C$ (where C is a constant dependent on the photometric band considered; e.g., Tananbaum et al. 1979; Maccacaro et al. 1988), is generally in the range [−1, 1]. Moreover, correlations have been found between X/O and the X-ray luminosity, mainly for obscured AGNs (Fiore et al. 2003; Marchesi et al. 2016); at any given X-ray luminosity, obscured AGNs are expected to have their UV/optical emission fainter than their unobscured counterparts, resulting in a higher X/O. Hence, we can further check the broad correspondence between HR and obscuration by investigating the behavior of the X/O as a function of hard-band luminosity, using the H-band intrinsic luminosity and i-band magnitude to compute X/O; we estimated $C = 5.03$ for the NDWFS i-band filter, although its exact value is not important, as it just shifts the whole figure to higher or lower values of X/O. In the right panel of Figure 17, we color-code sources based on their HR and visually demonstrate through their density contours that, in general, hard sources fall in the region of the plane where obscured AGNs are expected to be. Likewise, soft sources are more spread out, in particular at $L_{\rm X} > 10^{43}$ erg s^{-1}.

6.3. Intrinsic Luminosity

Having estimated $N_{\rm H}$ values using the HR–z plane, we computed the correction factor k, defined as the ratio between the obscured and intrinsic flux $k = f_{\rm obs}/f_{\rm int}$, where $f_{\rm int}$ is estimated with an unobscured power law with $\Gamma = 1.8$ following Marchesi et al. (2016). Since our $N_{\rm H}$ range is limited to $\log(N_{\rm H}/{\rm cm}^{-2}) \gtrsim 20$, we assigned $k = 1$ to those sources with $\log(N_{\rm H}/{\rm cm}^{-2}) \leqslant 20$. We translated 1σ uncertainties on the HR into uncertainties on the column density, which in turn constrained the minimum and maximum values of k for the lower and higher $N_{\rm H}$ limits, respectively.

Once we have calculated k for each band, we compute the rest-frame intrinsic flux $f_{\rm int}^{\rm RF} = f_{\rm int}\,(1+z)^{\Gamma-2}$ (with $\Gamma = 1.8$) and then, finally, the intrinsic luminosity at a given redshift using $L_{\rm int}^{\rm RF} = 4\pi D_L^2 f_{\rm int}^{\rm RF}$, where D_L is the luminosity distance.

A plot of the rest-frame intrinsic luminosity in the 2–10 keV band (converted from the 2–7 keV luminosity assuming $\Gamma = 1.8$) as a function of redshift is shown in the left panel of Figure 18. This panel demonstrates that the range of exposure times for observations in the Boötes field allows a relatively broad range of the luminosity–redshift plane to be explored. In particular, thanks to its combination of wide area and deep exposures, the CDWFS has sufficient statistical power to probe both above and below the knee of the luminosity function (L_*,

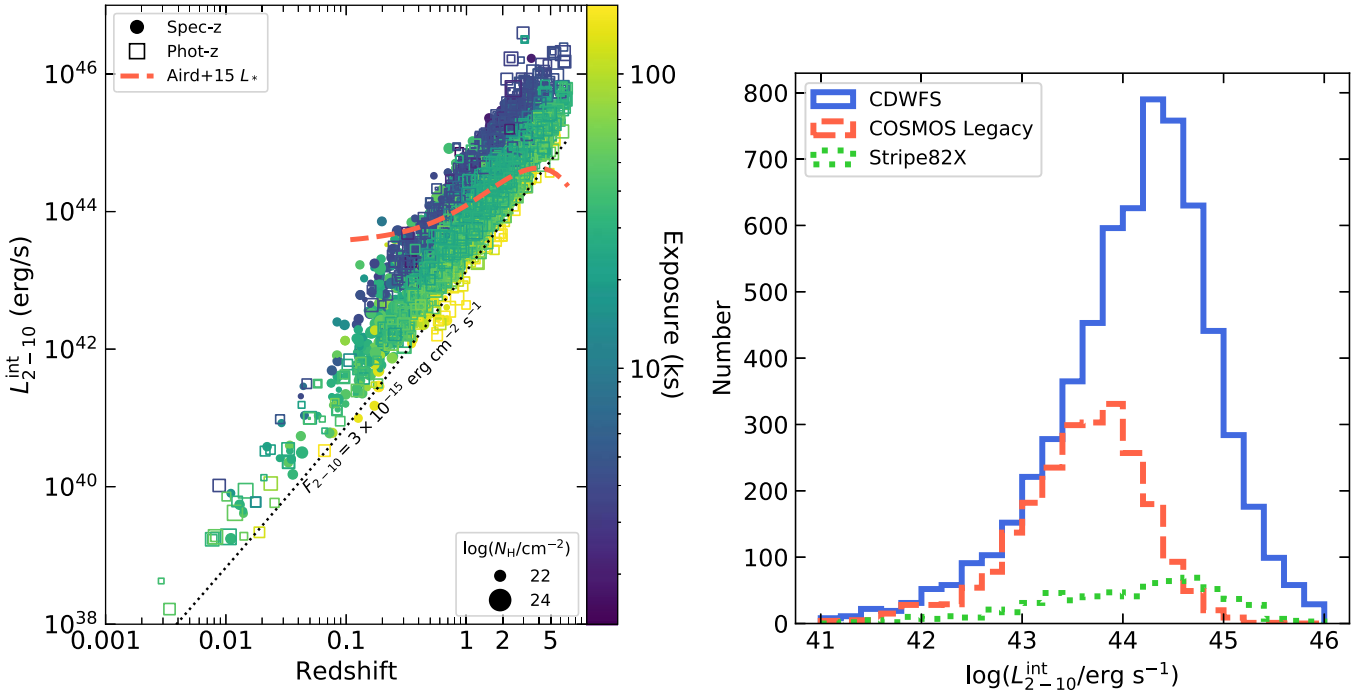

Figure 18. Left: intrinsic (i.e., corrected for absorption) rest-frame 2–10 keV luminosity as a function of redshift. Data points with spectroscopic/photometric redshifts are labeled as filled circles/open squares, respectively; their size is proportional to the $N_{\rm H}$ derived through the HR–z plane, and they are color-coded by exposure (in ks). The dotted line shows a flux of 3×10^{-15} erg cm^{-2} s^{-1}, while the red dashed line labels the evolution of the knee of the luminosity function (L_*) from Aird et al. (2015). Right: intrinsic rest-frame 2–10 keV luminosity distribution for CDWFS (solid blue histogram), COSMOS Legacy (dashed red histogram; Civano et al. 2016; Marchesi et al. 2016), and Stripe82X (dotted green histogram; LaMassa et al. 2016). With its unique features, CDWFS is a very valuable addition to the array of Chandra's Extragalactic Legacy Surveys, peaking at luminosities between the other two major wide surveys and providing excellent statistics.

as parameterized by Aird et al. 2015) in the redshift range $z \sim 0.5$–3. This is crucial to probe the full distribution of mass accretion rates for the AGN population over a large redshift range. This is even more evident when the distribution of rest-frame 2–10 keV luminosities for CDWFS, COSMOS Legacy (Civano et al. 2016; Marchesi et al. 2016), and Stripe82X (LaMassa et al. 2016) are compared, as demonstrated in the right panel of Figure 18. We show the 2–10 keV band luminosity, since it is less affected by obscuration corrections, but the situation is the same for the soft band. The combination of the wide area and the depth accumulated through 15 yr of Chandra observations makes CDWFS unique in terms of coverage. The CDWFS has more sources than the COSMOS Legacy and Stripe82X surveys combined at any luminosity. Furthermore, the distribution of CDWFS luminosities bridges the gap between COSMOS Legacy and Stripe82X, adding a significant number of sources in the luminosity range log(L/erg s^{-1}) ∼44–45. This is crucial to probe the typical and most luminous accreting black holes at the peak epoch of AGN and galaxy coevolution.

7. Catalog Description

The final X-ray catalog, which we release in electronic form, contains 6891 sources and a rich amount of information, with 102 columns. An extract of the first 10 sources can be found in Appendix B (Table B2).

The catalog is mainly divided into four sections.

1. Columns that are exclusively related to purely X-ray-derived quantities, such as coordinates, probabilities, counts, and fluxes.
2. Columns that start with the syntax "NDWFS_" are related to the NDWFS I-band catalog used by NWAY to look for I-band counterparts to X-ray sources.
3. Columns that start with the syntax "SDWFS_" are related to the SDWFS [3.6]-band catalog used by NWAY to look for [3.6]-band counterparts to X-ray sources.
4. Columns that are related to derived quantities, such as multiwavelength properties, redshift, column density, and intrinsic luminosity.

The breakdown of the columns of the catalog is as follows.

Column 1. ID of the X-ray source.

Columns 2–3. R.A. and decl. (J2000) of the X-ray source, in degrees.

Column 4. Positional error of the X-ray source, in arcseconds.

Column 5. F-band Poissonian probability that the source is a background fluctuation.

Column 6. F-band exposure-weighted average r_{90}, the approximate circular radius encompassing 90% of Chandra's PSF (in arcseconds). This radius was used to extract aperture photometry.

Column 7. F-band total counts within a circle of radius r_{90}.

Column 8. F-band background counts within a circle of radius r_{90}, extracted from our background maps at the position of the source.

Column 9. F-band net counts within a circle of radius r_{90} or a 3σ upper limit if the probability of the source being spurious is higher than the threshold.

Columns 10–11. Positive and negative errors on F-band net counts or -99 if the net counts are a 3σ upper limit.

Column 12. *F*-band total exposure in seconds at the position of the source.

Column 13. *F*-band net count rate in counts per second or a 3σ upper limit if the probability of the source being spurious is higher than the threshold.

Columns 14–15. Positive and negative errors on *F*-band net count rate or -99 if the net count rate is a 3σ upper limit.

Column 16. *F*-band flux or a 3σ upper limit if the probability of the source being spurious is higher than the threshold. The flux is obtained from the count rate (or its upper limit) by applying an aperture correction and the appropriate exposure-weighted ECF assuming $\Gamma = 1.4$.

Columns 17–18. Positive and negative errors on *F*-band flux or -99 if the flux is a 3σ upper limit.

Column 19. *S*-band Poissonian probability that the source is a background fluctuation.

Column 20. *S*-band exposure-weighted average r_{90}, the approximate circular radius encompassing 90% of Chandra's PSF (in arcseconds). This radius was used to extract aperture photometry.

Column 21. *S*-band total counts within a circle of radius r_{90}.

Column 22. *S*-band background counts within a circle of radius r_{90} extracted from our background maps at the position of the source.

Column 23. *S*-band net counts within a circle of radius r_{90} or a 3σ upper limit if the probability of the source being spurious is higher than the threshold.

Columns 24–25. Positive and negative errors on *S*-band net counts or -99 if the net counts are a 3σ upper limit.

Column 26. *S*-band total exposure in seconds at the position of the source.

Column 27. *S*-band net count rate in counts per second or 3σ upper limit if the probability of the source being spurious is higher than the threshold.

Columns 28–29. Positive and negative errors on *S*-band net count rate or -99 if the net count rate is a 3σ upper limit.

Column 30. *S*-band flux or a 3σ upper limit if the probability of the source being spurious is higher than the threshold. The flux is obtained from the count rate (or its upper limit) by applying an aperture correction and the appropriate exposure-weighted ECF assuming $\Gamma = 1.4$.

Columns 31–32. Positive and negative errors on *S*-band flux or -99 if the flux is a 3σ upper limit.

Column 33. *H*-band Poissonian probability that the source is a background fluctuation.

Column 34. *H*-band exposure-weighted average r_{90}, the approximate circular radius encompassing 90% of Chandra's PSF (in arcseconds). This radius was used to extract aperture photometry.

Column 35. *H*-band total counts within a circle of radius r_{90}.

Column 36. *H*-band background counts within a circle of radius r_{90} extracted from our background maps at the position of the source.

Column 37. *H*-band net counts within a circle of radius r_{90} or a 3σ upper limit if the probability of the source being spurious is higher than the threshold.

Columns 38–39. Positive and negative errors on *H*-band net counts or -99 if the net counts are a 3σ upper limit.

Column 40. *H*-band total exposure in seconds at the position of the source.

Column 41. *H*-band net count rate in counts per second or a 3σ upper limit if the probability of the source being spurious is higher than the threshold.

Columns 42–43. Positive and negative errors on *H*-band net count rate or -99 if the net count rate is a 3σ upper limit.

Column 44. *H*-band flux or a 3σ upper limit if the probability of the source being spurious is higher than the threshold. The flux is obtained from the count rate (or its upper limit) by applying an aperture correction and the appropriate exposure-weighted ECF assuming $\Gamma = 1.4$.

Columns 45–46. Positive and negative errors on the *H*-band flux or -99 if the flux is a 3σ upper limit.

Column 47. HR computed with BEHR (Park et al. 2006).

Columns 48–49. Positive and negative errors on HR.

Column 50. Index of the XBoötes counterpart in Kenter et al. (2005), -99 if no counterpart is found.

Column 51. Name of the XBoötes counterpart in Kenter et al. (2005), -99 if no counterpart is found.

Column 52. Distance in arcseconds between the CDWFS source and its XBoötes counterpart, -99 if no counterpart is found.

Column 53. Number of XBoötes counterparts associated within $1.1 \times r_{90}$ with the CDWFS source. Zero if no counterpart is found. If more than one XBoötes counterpart is found, the closest one was chosen.

Columns 54–55. J2000 R.A. and decl. coordinates for the *I*-band NDWFS counterpart, -99 if no counterpart in the *I* band is found.

Column 56. Vega *I*-band automatic magnitude ("MAG_AUTO") as computed by SExtractor (Bertin & Arnouts 1996), -99 if no NDWFS counterpart in the *I* band is found, 99 if *I*-band photometry is unreliable (see also the "FLAG_DEEP" entry).

Columns 57–58. J2000 R.A. and decl. coordinates for the [3.6]-band SDWFS counterpart, -99 if no counterpart in the [3.6] band is found.

Columns 59–66. Vega SDWFS magnitudes for the four IRAC channels and their uncertainties, -99 if no counterpart in the [3.6] band is found.

Column 67. SDWFS flag, -99 if no counterpart in the [3.6] band is found.

Column 68. Separation in arcseconds between the CDWFS source and its NDWFS counterpart, NULL if no counterpart in the *I* band is found.

Column 69. Separation in arcseconds between the CDWFS source and its SDWFS counterpart, NULL if no counterpart in the [3.6] band is found.

Column 70. Separation in arcseconds between the NDWFS and SDWFS counterparts, NULL if no counterpart is found in either of the two bands.

Column 71. Maximal separation in arcseconds between the CDWFS and its counterparts, 0.0 if no counterpart is found in either of the two bands.

Column 72. Number of catalogs in which the source is contained, with 1 meaning only CDWFS and 3 meaning CDWFS, NDWFS, and SDWFS.

Column 73. NWAY logarithm of the ratio between prior and posterior from distance matching.

Column 74. NWAY distance posterior probability comparing the association against no association.

Columns 75–76. NWAY bias factors coming from the additional *I*- and [3.6]-band magnitude information. If the magnitudes are unknown, the factors reduce to unity.

Column 77. Same as column 74 after additional information is added from the magnitude of the counterparts.

Column 78. NWAY `p_any` parameter. For each CDWFS entry, it represents the probability that one of the associations is the correct one. As stated in the NWAY manual, a low value of this parameter does not rule out the associated counterpart; it can simply mean that there is not enough information to declare it secure.

Column 79. Spectroscopic redshift from the AGES catalog, −99 if no spectroscopic redshift is available.

Column 80. Photometric redshift estimate from the Duncan et al. (2020, submitted) catalog, obtained through fitting of the spectral energy distribution (SED) with a hybrid template + machine-learning technique; −99 if no counterpart is found. Specifically, we provide the median of the primary redshift peak above the 80% highest probability density (HPD) credible interval (CI) for the photometric redshift posterior.

Columns 81–82. Minimum and maximum of the primary peak above the 80% HPD CI (column 80) from the Duncan et al. (2020, submitted) catalog, obtained through SED fitting with a hybrid template + machine-learning technique; −99 if no counterpart is found.

Column 83. "FLAG_DEEP" = 1 indicates that the NDWFS source has good data that can go to the full depth of the $B_{\rm wRI}$ optical images. This flag excludes bad pixels, bleed trails, bright star halos, and bright galaxies; −99 if no counterpart is found.

Column 84. Index of the source in the Duncan et al. (2020, submitted) catalog.

Column 85. Best redshift: spectroscopic redshift when available, photometric otherwise, −99 if no redshift is available.

Column 86. Redshift flag: 1 if the best redshift is spectroscopic, 0 if it is photometric, −99 if no redshift is available.

Columns 87–89. Logarithm of the column density estimated from fitting the HR–z plane using the best redshift and positive and negative uncertainties. Note that the uncertainties reflect the HR ones only, while the redshift is fixed. The minimum value is 20, while it is −99 if no column density was computed (due to a missing redshift).

Columns 90–98. Correction factors k with their maximal and minimal values for the three Chandra bands. The correction factor is defined as the ratio between the observed (obscured) flux and the unobscured one. The maximal and minimal values reflect the maximal and minimal column density estimates. Unity values mean that the source has $\log(N_{\rm H}/{\rm cm}^{-2}) \leqslant 20$ and is considered unobscured, −99 if no redshift is available.

Columns 99–101. Deabsorbed rest-frame luminosities in the *F*, *S*, and *H* bands obtained from the absorption-corrected fluxes and assuming $\Gamma = 1.8$; −99 if no redshift is available or $z = 0$.

Column 102. Deabsorbed rest-frame luminosity in the 2–10 keV band obtained from the absorption-corrected *H*-band luminosity and assuming $\Gamma = 1.8$; −99 if no redshift is available or $z = 0$.

8. Summary and Conclusions

In this paper, we presented a detailed overview of the CDWFS, a new ambitious Chandra survey in the Boötes field. The information about the release of the associated data products can be found in Appendix C. The CDWFS is comprised of 281 Chandra observations in the Boötes field spanning 15 yr of observations, for a total observing time of 3.4 Ms.

To analyze this large data set in a homogeneous way, we built accurate simulations of the whole field, taking into account the change of the instrument over the years. The resulting catalog of 6891 X-ray point sources has a spurious fraction of sources of ∼1% in each band. Taking into account this spurious fraction, together with source incompleteness and Eddington bias, accurate number counts were derived. This analysis confirmed the presence of an overdensity of hard X-ray sources in the corner of the Boötes field that has the deepest observations (i.e., the LaLa survey field), as previously noted by Wang et al. (2004). The large number of X-ray sources detected corresponds to a resolved fraction of the CXB of 65.0% ± 12.8% between 0.5 and 2 keV and 81.0% ± 11.5% between 2 and 7 keV.

The wealth of multiwavelength data in the Boötes field allowed us to assign redshifts to ∼94% of our sources. We then used the HR–redshift plane to derive estimates of obscuration and intrinsic luminosities for our sources. The unique and homogeneous coverage of the luminosity–redshift parameter space for CDWFS sources, together with the extensive multiwavelength coverage of the Boötes field, makes the CDWFS a valuable addition to the Chandra X-ray legacy surveys. In particular, the catalog that we present and release in this paper is ideal for investigating AGN–galaxy coevolution at the cosmic epoch where AGN activity and star formation are most concurrent.

We thank the anonymous referee for a thorough report that helped to strengthen the paper and make it clearer.

This research has made (heavy) use of new data obtained by the Chandra X-ray Observatory and data obtained from the Chandra Data Archive, as well as software provided by the Chandra X-ray Center (CXC).

A.M. and R.C.H. acknowledge support by the NSF through grant No. 1554584 and NASA through grant No. NNX15AP24G and Chandra GO award GO7-18130X. R.J.A. was supported by FONDECYT, grant No. 1191124. S.C. acknowledges financial support from the Department of Science and Technology through the SERB Early Career Research grant and Presidency University through the Faculty Research and Professional Development Funds. The work of P.R.M.E. and D.S. was carried out at the Jet Propulsion Laboratory, California Institute of Technology, under a contract with NASA. K.J.D. acknowledges support from the ERC Advanced Investigator program NewClusters 321271.

Facilities: CXO, KPNO:2.1 m, Mayall, MMT, Spitzer.

Software: CIAO (Fruscione et al. 2006), XSPEC (Arnaud 1996), NWAY (Salvato et al. 2018), Astropy (Astropy Collaboration et al. 2013, 2018).

Appendix A
NDWFS, SDWFS, and Gaia Astrometry

As explained in the main text, all 281 Chandra observations included in this paper have been realigned to a common astrometric reference. In particular, we pinned the new aspect solutions of all observations to the USNO-A2 astrometry using the catalog of NDWFS optical counterparts to XBoötes sources

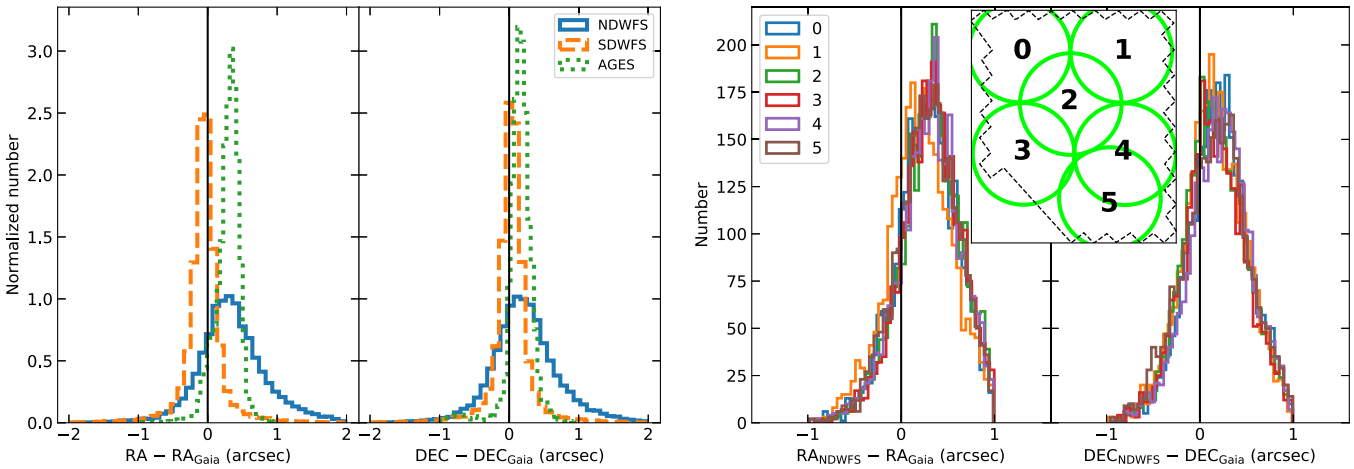

Figure A1. Left: NDWFS (solid blue histogram), AGES (dotted green histogram), and SDWFS (dashed orange histogram) astrometry compared to Gaia. Unlike SDWFS, NDWFS and AGES show a systematic shift with respect to Gaia. Right: NDWFS astrometric shift with respect to Gaia for the six partially overlapping regions highlighted in the inset. To be even more conservative about possible wrong associations, we matched sources within 1″.

(Brand et al. 2006). This procedure was chosen to simplify the matching before a careful source detection. However, given that the Gaia mission is now the new astrometric reference, we made sure that all of the observations and catalogs used in this work refer to the same astrometric system.

To this aim, we cross-matched the Gaia DR2 catalog (Gaia Collaboration et al. 2018) to the USNO-A2 and SDWFS catalogs using a circle of 2° radius centered on R.A. = 218.0 deg and decl. = +34.0 deg. As shown in the left panel of Figure A1, while the SDWFS coordinates did not show any systematic shift with respect to Gaia, the NDWFS and AGES ones (both referring to the USNO-A2 WCS) appeared to be shifted by ΔR.A. = 0.″32 and Δdecl. = 0.″20. A similar shift was noticed between NDWFS and SDSS by Cool (2007). We verified that this systematic effect is consistent throughout the field, splitting up the Boötes field into six partially overlapping circular regions of 0.8 deg radius. In Figure A1, we show how the shifts compare among regions, demonstrating that all regions show the same systematic shift in decl. and all but one show it in R.A. (region 1 shows a slightly smaller offset in R.A.).

Hence, we decided to shift all CDWFS mosaics used for subsequent analysis by the same amount, defining the new CRVAL1 and CRVAL2 header keywords as

$$\begin{aligned}&\text{CRVAL1, new} = \text{CRVAL1, old} - 8.927566 \times 10^{-5}\ \text{degrees},\\&\text{CRVAL2, new} = \text{CRVAL2, old} - 5.610275 \times 10^{-5}\ \text{degrees}.\end{aligned} \tag{A1}$$

Appendix B
Tables of the Excluded XBoötes Sources and the Main Catalog

Table B1 shows an extract of the first 10 rows of the additional list of XBoötes sources not included in the CDWFS catalog, while Table B2 gives an extract (with a few selected columns) of the first 10 rows of the main catalog released with

Table B1
Extract of the Table with Information on the Excluded XBoötes Sources

CXOXB	ID	R.A. (deg)	Decl. (deg)	PROB_*F*	R90_*F* (arcsec)	TOT_*F*	BKG_*F*	EXP_*F* (s)	PROB_*S*	R90_*S* (arcsec)	TOT_*S*	BKG_*S*	EXP_*S* (s)	PROB_*H*	R90_*H* (arcsec)	TOT_*H*	BKG_*H*	EXP_*H* (s)
J142420.5+333922	1	216.08566	33.65609	0.0849	15.62	4.0	1.94	3243	0.3428	15.62	1.0	0.67	3097	0.1138	16.42	3.0	1.41	3202
J142438.1+334245	14	216.15904	33.71254	0.0043	8.44	4.0	0.67	4124	0.0223	8.44	2.0	0.24	4061	0.0829	9.24	2.0	0.53	4097
J142440.4+351921	18	216.16857	35.32244	0.0008	7.07	4.0	0.41	3903	0.0005	7.07	3.0	0.15	3889	0.2326	7.87	1.0	0.32	3863
J142448.6+334540	43	216.20241	33.76126	0.0001	7.37	5.0	0.47	3624	0.0006	7.37	3.0	0.17	3583	0.0416	8.17	2.0	0.34	3653
J142449.8+351815	50	216.20757	35.30437	4.1×10^{-5}	4.41	4.0	0.19	4387	0.0023	4.41	2.0	0.07	4382	0.0088	5.21	2.0	0.14	4346
J142451.7+351411	56	216.21541	35.23646	0.0002	5.75	4.0	0.28	4143	0.0960	5.75	1.0	0.11	4106	0.0016	6.55	3.0	0.23	4091
J142457.9+333318	67	216.24154	33.55514	3.5×10^{-5}	8.17	6.0	0.60	4056	0.1708	8.17	1.0	0.21	3935	0.0001	8.97	5.0	0.49	4072
J142504.4+355015	83	216.26836	35.83769	7.6×10^{-5}	7.30	5.0	0.43	3980	0.0074	7.30	2.0	0.13	3985	0.0054	8.10	3.0	0.36	3950
J142504.5+355125	84	216.26879	35.85704	0.0054	9.16	4.0	0.72	4331	0.0192	9.16	2.0	0.22	4307	0.0190	9.96	3.0	0.59	4332
J142505.6+351303	89	216.27333	35.21770	4.1×10^{-5}	4.54	4.0	0.19	4344	5.3×10^{-5}	4.54	3.0	0.07	4344	0.1335	5.34	1.0	0.16	4330

Note. The *F*, *S*, and *H* subscripts refer to the *F*, *S*, and *H* bands, respectively. The ID column refers to the number of the source in the Kenter et al. (2005) catalog. The full version of the list can be found in the electronic version of the catalog.
(This table is available in its entirety in FITS format.)

Table B2
Extract of the Main Source Catalog Table

R.A. (J2000) (deg)	Decl. (J2000) (deg)	POS_ERR (arcsec)	FLUX_*F* (erg cm^{-2} s^{-1})	HR	XB_ID	NDWFS_R.A. (deg)	NDWFS_decl. (deg)	I_MAG_AUTO (mag)	SDWFS_R.A. (deg)	SDWFS_decl. (deg)	SDWFS_CH1_MA (mag)	ZSP	ZPH	LOG_NH (cm^{-2})	LINT_*F* (erg s^{-1})
218.09335	32.30161	2.12	2.70×10^{-14}	−0.808	1999	−99	−99	−99	218.09415	32.30075	15.17	−99	−99	−99	−99
216.33986	32.31454	1.22	3.79×10^{-14}	0.065	170	−99	−99	−99	216.33987	32.3142	18.31	−99	3.1321	23.58	4.46×10^{45}
217.67761	32.32548	0.80	1.17×10^{-13}	−0.608	1552	217.67748	32.32556	18.45	217.67758	32.32557	15.40	−99	0.4135	20.0	6.64×10^{43}
217.97970	32.34356	1.51	1.37×10^{-14}	0.390	1872	217.97991	32.34344	23.06	217.97999	32.34352	17.34	−99	1.8089	23.48	5.69×10^{44}
217.63251	32.36268	0.50	6.55×10^{-14}	−0.544	1508	217.63243	32.36277	18.52	217.63245	32.36276	15.61	−99	2.0131	21.54	1.60×10^{45}
217.11544	32.37076	1.34	1.13×10^{-14}	0.908	953	217.11581	32.37097	23.73	217.11576	32.37104	17.96	−99	1.899	24.06	1.03×10^{45}
218.05901	32.37461	1.32	8.57×10^{-15}	−0.867	−99	218.05898	32.37503	23.94	218.05907	32.3751	16.97	−99	1.6338	20.0	1.24×10^{44}
216.71267	32.37187	1.0	1.59×10^{-14}	0.934	508	216.71255	32.37172	19.74	216.71231	32.3719	15.44	−99	0.7764	23.48	1.46×10^{44}
216.28777	32.37006	1.11	1.17×10^{-14}	0.643	105	216.28766	32.36974	23.51	216.28759	32.36986	18.47	−99	2.0223	23.8	8.17×10^{44}
217.72037	32.37844	1.66	1.25×10^{-14}	−0.162	1589	217.72128	32.37761	25.15	−99	−99	−99	−99	1.0886	22.52	1.03×10^{44}

Note. The full electronic catalog, accessible through the online journal, contains many more columns, which are described in Section 7.
(This table is available in its entirety in FITS format.)

this paper. Both full catalogs can be found in the electronic version of the paper.

Appendix C
Public Data Products Associated with This Paper

This paper publicly releases three catalogs:

1. the log of the 281 Chandra observations considered in this work (see Table 1),
2. the list of the 394 XBoötes sources not appearing in the main catalog (see Table B1), and
3. the main catalog containing 6891 sources (see Table B2).

In addition, all of the data products described in Section 2 and the raw merged catalog returned by `wavdetect` (i.e., before reliability cuts) are available upon request.

ORCID iDs

Alberto Masini https://orcid.org/0000-0002-7100-9366
Ryan C. Hickox https://orcid.org/0000-0003-1468-9526
Christopher M. Carroll https://orcid.org/0000-0003-3574-2963
James Aird https://orcid.org/0000-0003-1908-8463
David M. Alexander https://orcid.org/0000-0002-5896-6313
Roberto J. Assef https://orcid.org/0000-0002-9508-3667
Richard Bower https://orcid.org/0000-0002-5215-6010
Mark Brodwin https://orcid.org/0000-0002-4208-798X
Michael J. I. Brown https://orcid.org/0000-0002-1207-9137
Suchetana Chatterjee https://orcid.org/0000-0002-3236-2853
Chien-Ting J. Chen https://orcid.org/0000-0002-4945-5079
Arjun Dey https://orcid.org/0000-0002-4928-4003
Michael A. DiPompeo https://orcid.org/0000-0001-6788-1701
Kenneth J. Duncan https://orcid.org/0000-0001-6889-8388
William R. Forman https://orcid.org/0000-0002-9478-1682
Anthony H. Gonzalez https://orcid.org/0000-0002-0933-8601
Andrew D. Goulding https://orcid.org/0000-0003-4700-663X
Kevin N. Hainline https://orcid.org/0000-0003-4565-8239
Buell T. Jannuzi https://orcid.org/0000-0002-1578-6582
Christopher S. Kochanek https://orcid.org/0000-0001-6017-2961
Ralph Kraft https://orcid.org/0000-0002-0765-0511
Kyoung-Soo Lee https://orcid.org/0000-0003-3004-9596
Eric D. Miller https://orcid.org/0000-0002-3031-2326
James Mullaney https://orcid.org/0000-0002-3126-6712
Andrew Ptak https://orcid.org/0000-0001-5655-1440
Daniel Stern https://orcid.org/0000-0003-2686-9241
Alexey Vikhlinin https://orcid.org/0000-0001-8121-0234
David A. Wake https://orcid.org/0000-0002-6047-1010

References

Aird, J., Alexander, D. M., Ballantyne, D. R., et al. 2015, ApJ, 815, 66
Arnaud, K. A. 1996, in ASP Conf. Ser. 101, Astronomical Data Analysis Software and Systems V, ed. G. H. Jacoby & J. Barnes (San Francisco, CA: ASP), 17
Ashby, M. L. N., Stern, D., Brodwin, M., et al. 2009, ApJ, 701, 428
Astropy Collaboration, Price-Whelan, A. M., Sipőcz, B. M., et al. 2018, AJ, 156, 123
Astropy Collaboration, Robitaille, T. P., Tollerud, E. J., et al. 2013, A&A, 558, A33
Bertin, E., & Arnouts, S. 1996, A&AS, 117, 393
Bian, F., Fan, X., Jiang, L., et al. 2013, ApJ, 774, 28
Bianchi, S., & Guainazzi, M. 2007, in AIP Conf. Ser. 924, The Multicolored Landscape of Compact Objects and Their Explosive Origins, ed. T. di Salvo et al. (Melville, NY: AIP), 822
Brand, K., Brown, M. J. I., Dey, A., et al. 2006, ApJ, 641, 140
Brandt, W. N., & Alexander, D. M. 2015, A&ARv, 23, 1
Brown, M. J. I., Dey, A., Jannuzi, B. T., et al. 2007, ApJ, 654, 858
Brusa, M., Civano, F., Comastri, A., et al. 2010, ApJ, 716, 348
Brusa, M., Comastri, A., Daddi, E., et al. 2005, A&A, 432, 69
Brusa, M., Zamorani, G., Comastri, A., et al. 2007, ApJS, 172, 353
Civano, F., Marchesi, S., Comastri, A., et al. 2016, ApJ, 819, 62
Cool, R. J. 2007, ApJS, 169, 21
Coppejans, R., Cseh, D., Williams, W. L., van Velzen, S., & Falcke, H. 2015, MNRAS, 450, 1477
De Luca, A., & Molendi, S. 2004, A&A, 419, 837
de Vries, W. H., Morganti, R., Röttgering, H. J. A., et al. 2002, AJ, 123, 1784
Duncan, K. J., Brown, M. J. I., Williams, W. L., et al. 2018a, MNRAS, 473, 2655
Duncan, K. J., Kondapally, R., & Brown, M. J. I. 2020, A&A, submitted
Duncan, K. J., Jarvis, M. J., Brown, M. J. I., & Röttgering, H. J. A. 2018b, MNRAS, 477, 5177
Eddington, A. S. 1913, MNRAS, 73, 359
Eisenhardt, P. R., Stern, D., Brodwin, M., et al. 2004, ApJS, 154, 48
Elvis, M., Civano, F., Vignali, C., et al. 2009, ApJS, 184, 158
Event Horizon Telescope Collaboration, Akiyama, K., Alberdi, A., et al. 2019, ApJL, 875, L1
Fabian, A. C. 2012, ARA&A, 50, 455
Ferrarese, L., & Merritt, D. 2000, ApJL, 539, L9
Fiore, F., Brusa, M., Cocchia, F., et al. 2003, A&A, 409, 79
Fruscione, A., McDowell, J. C., Allen, G. E., et al. 2006, Proc. SPIE, 6270, 62701V
Gaia Collaboration, Brown, A. G. A., Vallenari, A., et al. 2018, A&A, 616, A1
Gaia Collaboration, Prusti, T., de Bruijne, J. H. J., et al. 2016, A&A, 595, A1
Gebhardt, K., Bender, R., Bower, G., et al. 2000, ApJL, 539, L13
Gehrels, N. 1986, ApJ, 303, 336
Georgakakis, A., Nandra, K., Laird, E. S., Aird, J., & Trichas, M. 2008, MNRAS, 388, 1205
Ghez, A. M., Salim, S., Weinberg, N. N., et al. 2008, ApJ, 689, 1044
Gonzalez, A. H., Brodwin, M., Brown, M. J. I., et al. 2010, AAS Meeting, 216, 415.13
Häring, N., & Rix, H.-W. 2004, ApJL, 604, L89
Harrison, C. M. 2017, NatAs, 1, 0165
Hickox, R. C., & Alexander, D. M. 2018, ARA&A, 56, 625
Hickox, R. C., Jones, C., Forman, W. R., et al. 2009, ApJ, 696, 891
Hickox, R. C., & Markevitch, M. 2006, ApJ, 645, 95
Jannuzi, B., Weiner, B., Block, M., et al. 2010, AAS Meeting, 215, 470.01
Jannuzi, B. T., & Dey, A. 1999, in ASP Conf. Ser. 191, The NOAO Deep Wide-Field Survey, ed. R. Weymann et al. (San Francisco, CA: ASP), 111
Kalberla, P. M. W., Burton, W. B., Hartmann, D., et al. 2005, A&A, 440, 775
Kenter, A., Murray, S. S., Forman, W. R., et al. 2005, ApJS, 161, 9
Kim, M., Kim, D.-W., Wilkes, B. J., et al. 2007a, ApJS, 169, 401
Kim, M., Wilkes, B. J., Kim, D.-W., et al. 2007b, ApJ, 659, 29
Kochanek, C. S., Eisenstein, D. J., Cool, R. J., et al. 2012, ApJS, 200, 8
Kormendy, J. 2004, in Coevolution of Black Holes and Galaxies, ed. L. C. Ho (Cambridge: Cambridge Univ. Press), 1
Kormendy, J., & Ho, L. C. 2013, ARA&A, 51, 511
Kormendy, J., & Richstone, D. 1995, ARA&A, 33, 581
Kozłowski, S., Kochanek, C. S., Ashby, M. L. N., et al. 2016, ApJ, 817, 119
Kozłowski, S., Kochanek, C. S., Stern, D., et al. 2010, ApJ, 716, 530
Kuo, C. Y., Braatz, J. A., Condon, J. J., et al. 2011, ApJ, 727, 20
Laird, E. S., Nandra, K., Georgakakis, A., et al. 2009, ApJS, 180, 102
LaMassa, S. M., Urry, C. M., Cappelluti, N., et al. 2016, ApJ, 817, 172
Lambrides, E. L., Chiaberge, M., Heckman, T., et al. 2020, ApJ, 897, 160
Lehmer, B. D., Xue, Y. Q., Brandt, W. N., et al. 2012, ApJ, 752, 46
Li, J., Xue, Y., Sun, M., et al. 2019, ApJ, 877, 5
Luo, B., Brandt, W. N., Xue, Y. Q., et al. 2017, ApJS, 228, 2
Maccacaro, T., Gioia, I. M., Wolter, A., Zamorani, G., & Stocke, J. T. 1988, ApJ, 326, 680
Madau, P., & Dickinson, M. 2014, ARA&A, 52, 415
Magorrian, J., Tremaine, S., Richstone, D., et al. 1998, AJ, 115, 2285
Marchesi, S., Civano, F., Elvis, M., et al. 2016, ApJ, 817, 34
Markevitch, M., Bautz, M. W., Biller, B., et al. 2003, ApJ, 583, 70
Murray, S. S., Kenter, A., Forman, W. R., et al. 2005, ApJS, 161, 1

Nandra, K., Laird, E. S., Adelberger, K., et al. 2005, MNRAS, 356, 568
Nandra, K., Laird, E. S., Aird, J. A., et al. 2015, ApJS, 220, 10
Oliver, S. J., Bock, J., Altieri, B., et al. 2012, MNRAS, 424, 1614
Park, T., Kashyap, V. L., Siemiginowska, A., et al. 2006, ApJ, 652, 610
Puccetti, S., Vignali, C., Cappelluti, N., et al. 2009, ApJS, 185, 586
Retana-Montenegro, E., Röttgering, H. J. A., Shimwell, T. W., et al. 2018, A&A, 620, A74
Ricci, C., Bauer, F. E., Treister, E., et al. 2017, MNRAS, 468, 1273
Ross, E., & Chaplin, W. J. 2019, SoPh, 294, 8
Salvato, M., Buchner, J., Budavári, T., et al. 2018, MNRAS, 473, 4937
SILSO World Data Center 2002–2018, International Sunspot Number Monthly Bulletin and Online Catalog http://www.sidc.be/silso/
Slavin, J. D., Wargelin, B. J., & Koutroumpa, D. 2013, ApJ, 779, 13
Tananbaum, H., Avni, Y., Branduardi, G., et al. 1979, ApJL, 234, L9
van Weeren, R. J., Williams, W. L., Tasse, C., et al. 2014, ApJ, 793, 82
Wang, J. X., Malhotra, S., Rhoads, J. E., et al. 2004, AJ, 127, 213
Wilkes, B. J., Kuraszkiewicz, J., Haas, M., et al. 2013, ApJ, 773, 15
Williams, W. L., Intema, H. T., & Röttgering, H. J. A. 2013, A&A, 549, A55
Xue, Y. Q. 2017, NewAR, 79, 59
Xue, Y. Q., Luo, B., Brandt, W. N., et al. 2011, ApJS, 195, 10